UNIVERSITY OF CALIFORNIA

SANTA CRUZ

THE FORMATION AND EVOLUTION OF r-PROCESS PROGENITORS

A dissertation submitted in partial satisfaction of the
requirements for the degree of

DOCTOR OF PHILOSOPHY

in

ASTRONOMY AND ASTROPHYSICS

by

Phillip Macias

June 2019

The Dissertation of Phillip Macias
is approved:

_____

Enrico Ramirez-Ruiz, Chair

_____

Ryan J. Foley

_____

Daniel Kasen

_____

Lori Kletzer
Vice Provost and Dean of Graduate Studies

Table of Contents

List of Figures

Abstract

The Formation and Evolution of r-Process Progenitors

by

Phillip Macias

Neutron stars are amongst the most compact and exotic objects in the universe. When born in pairs, their eventual merging is responsible for some of the most energetic phenomena and plays a significant role in the chemical evolution of galaxies. This thesis combines analytical calculations with observations of stellar abundances to gain further insight into how these binaries are formed and the nucleosynthesis that takes place once they eventually merge under the influence of gravitational radiation.

We derive a relation between key parameters governing the process of bringing neutron stars to separations at which they are able to merge within a Hubble time. We also examine the conditions at the onset of a stellar merger through detailed stellar modeling of an observed progenitor system. We utilize observed stellar abundances to place stringent constraints on the progenitor site of r-process nucleosynthesis and find it to be consistent with expectations from neutron star mergers. We further utilize these stellar abundances to place constraints on another proposed site of the r-process , namely the collapsar, and find the abundances to be in tension with theoretical predictions of the model. Finally, we use stellar abundances to make predictions of future electromagnetic transients to be detected from these mergers and to test their viability as an r-process production mechanism throughout cosmic time.

To my mother and grandmother, whose unwavering love and support are with me each and every day.

Acknowledgments

As I sit here in my living room, there is a part of me that can not believe I am typing this. It is difficult to overstate how surreal it feels to look back on the culmination of so many years of my life. I grew up not knowing a single person who had taken their pursuit of academic knowledge beyond high school, let alone delving into the depths of a doctorate in a specific subject. At the end of my time in high school, I did not have an inkling of thought as to where I would end up next. I serendipitously found physics and astronomy during my early years of undergraduate education, and was invited to conduct research within the, at the time, incipient group of Dr. Joshua Smith at Cal State Fullerton. This invitation proved to be immeasurably meaningful, and for that I am forever grateful.

Entering graduate school, it would make sense that I might have felt a sense of alienation due to my lack of family experience in higher education, which I imagine some of my colleagues have been able to recount and possibly fall back upon in times of stress. However this was rarely the case; I have made many of my best friends throughout this time. My cohort of Zach, Jieun, Camille, Alex, and Marie have helped me through many homework sets and test preparation sessions where our collaborative efforts easily turned what should be a fretful night into an example of what makes me so excited to be a part of this field.

My friends who entered the program in subsequent years have also added a great deal of joy to my time here. Emily and Alexa, I cannot thank you enough for the support you have provided me, whether in the form of a dinner collaboration or a drink at the end of the week at El Palomar. Chris, you have and will always be my best friend. You know that already so I won't gab on, but I am so grateful for all the joy and laughter you've brought into my life for almost a decade. I am very lucky to have been surrounded by such amazing colleagues and friends.

as a mentor, role model, and collaborator during my earlier years of graduate school and for permitting me to include pieces of work we have done together in this thesis.

I wish to acknowledge my loved ones who have accepted and helped shape me throughout my life. Marthe, you have helped me throughout this process and for that I can not thank you enough. Your knowledge and kindness have been instrumental throughout my time in school. My family has been an incredible support system and I thank my father and sister for always being there for me. To my mother and grandmother, I will always know you as my "biggest fans" and will continue to utilize the motivation that brings me through any trying times ahead. I am abundantly privileged to have these people in my life.

Chapter 1

Introduction

The study of compact object binaries is in the midst of a renaissance due to LIGO's ongoing observing runs, which continue to advance the burgeoning field of multi-messenger astronomy by shedding light on open questions and challenging theoretical expectations. Concurrently, large photometric surveys such as ZTF and ASAS-SN are beginning to probe transients in unexplored regions of parameter space, with LSST soon to follow. The inevitable combination of gravitional wave (GW) and electromagnetic (EM) data synergistically has promised to revolutionize the way we understand interactions between the most exotic objects in the universe and has delivered bountifully thus far.

This realization has spurred a huge effort on the theoretical front in recent years in order to prepare for these GW observations in addition to any possible EM counterparts and effectively interpret them as they are detected by LIGO and EM telescopes. Two of the outstanding theoretical issues which have and will continue to be constrained within the coming years are the formation scenarios of these binaries as well as the role of binaries containing at least one NS in the formation of the heaviest elements. We outline in more detail the background and outstanding questions regarding these questions below.

1.1 Common Envelope Evolution

It is now known that binary stars are not rare and most massive stars are born with a companion (e.g. Duchêne & Kraus, 2013). As the stars burn through their nuclear fuel, expansion inevitably occurs often resulting in some type of interaction. Depending on the binary parameters, this interaction may or may not be stable. In the case of unstable mass transfer, it is possible for a one star to completely engulf another, resulting in a common envelope phase. The engulfed secondary may be able to remove the enshrouding envelope, largely at the cost of the orbital binding energy. This tightening of the resultant binary is a major progenitor channel for systems which will merge due to gravitational radiation and be detected by LIGO, known as the classical formation channel.

Though the qualitative picture of this interaction has been understood since the work of Paczynski (1976), a full quantitative understanding of the picture remains elusive. This is largely due to the extreme dynamic range amongst both temporal and physical scales (e.g. Ivanova et al., 2013). Physically, the scales range from the size of the compact object of interest, often a neutron star, to the size of a giant star. Temporally, the timescales of interest range from the nuclear timescale of the engulfing star to the dynamical time of the flowing gas near the embedded object. In addition, the role of recombination energy (Ivanova et al., 2015), the structure and response of the engulfing star (Kruckow et al., 2016), the ability of convection to radiate binding energy (Wilson & Nordhaus, 2019), and the relevance of jets launched by the engulfed star (Murguia-Berthier et al., 2017; Soker, 2017) have yet to be fully understood.

For these reasons, global simulations of a compact object embedded within a giant star which are able to capture all of the relevant physics and scales remain computationally infeasible. Within our group we have instead chosen to dedicate

2

our efforts toward another crucial aspect of these interactions, the flow morphology close to the embedded object. With these "zoom in" common envelope simulations, we circumvent the unsolved question of envelope ejection mechanisms and instead focus on other physical quantities of interest such as the accretion rate onto the compact object and the drag experienced by it (MacLeod & Ramirez-Ruiz, 2015). The flow morphology near the compact object is responsible for determining these quantities and depends critically, as we describe in Chapter 2, on the Mach number of the flow and the local density gradient. This smaller scale view of the interaction may then be implemented as a sub-grid calculation in larger global simulations, furthering our understanding of this elusive but crucial phase of binary interaction.

While common envelope encounters have proven difficult to observe in nature, we are now beginning to gain insight into the onset of unstable mass transfer and the resultant stellar mergers through luminous red novae. These result from the mergers of lower mass stars, and while the physics may not be directly applicable to the case of a compact object being embedded in a giant star, these serve as the first observational clues as to how a common envelope event may begin.

1.2 r-process Nucleosynthesis

As first detailed in the landmark paper by Burbidge et al. (1957), massive stellar evolution efficiently synthesizes most of the heavy elements up to Fe, enriching the surrounding interstellar medium through their subsequent supernovae (SNe) and contributing to the chemical evolution of the galaxy. Synthesis of elements more massive than Fe is an endothermic reaction and requires more exotic nucleosynthetic pathways involving bombardment of nuclei with protons or neutrons. The process of rapid neutron capture, known as the r-process , is responsible for the creation of roughly half of the elements more massive than Fe and was origi-

nally thought to take place in core-collapse supernovae (CCSNe, Burbidge et al., 1957), where a newborn NS was proposed as a source that would provide the rapid neutron flux required. This was not the only proposed mechanism, as Lattimer & Schramm (1974a) proposed an alternative scenario in which a NS would be tidally disrupted immediately prior to it merging with a stellar mass BH. The unbound material would also provide the neutron flux necessary to bombard seed nuclei and create the heaviest elements in the universe.

For decades astronomers have debated the viability of both proposed progenitor systems, with CCSNe long being the preferred mechanism. One criterion which must be satisfied by either model is to match the average production rate of r-process elements throughout the history of the Milky Way. This number may be easily calculated to order of magnitude by assuming all stars have an r-process mass comparable to that of the sun, $\approx 3 \times 10^{-7}$ $M_\odot$ (Arnould et al., 2007). Multiplying this mass by the number of stars in the MW and dividing through by its age thus yields an average production rate of $\approx 10^{-7}$ $M_\odot$ yr^{-1}.

Early CCSN simulations yielded total r-process masses on the order of 10^{-5} $M_\odot$, which when multiplied by an average rate in the MW of 10^{-2} yr^{-1} would be able to supply the bulk of the r-process mass seen today. However, simulations of NSBH and NSNS mergers yield much higher masses for a single event, on the order of 10^{-2} $M_\odot$, which are also able to satisfy this constraint given their average galactic rate of 10^{-5} yr^{-1}. This degeneracy between rate and mass per event served as a major reason for the debate to linger for decades.

1.2.1 Indirect Observational Constraints on r-process Progenitors

Pieces of indirect evidence regarding the birth sites of heavy elements have begun to emerge over the years through observations of their abundances in stars. When stars form, they serve mostly as a snapshot in time of the ISM from which they have been composed. This is the foundational principle upon which the field of chemical evolution was built, in which models are made of how the galaxy enriches across decades of [Fe/H] metallicity, where [Fe/H] = $\log_{10}(N_{\mathrm{Fe}}/N_{\mathrm{H}}) - \log_{10}(N_{\mathrm{Fe}}/N_{\mathrm{H}})_{\odot}$, and N_{Fe} is the column density of a given element. These models are then tested by observations of stellar abundances. Going from an observed spectrum to an inference of the mass fraction of an element requires many individual pieces of physics, including knowing where a given line should exist, modeling of the stellar atmosphere in which that element was observed, and being aware of possible deviations from local thermodynamical equilibrium.

While chemical evolution models which track enrichment over time have greatly increased our knowledge of various nucleosynthetic progenitor channels and their properties such as delay-time distributions and yields, the r-process component of my thesis largely makes use of the metal poor stars which are formed early in the history of the galaxy. The sun, for example, was formed at a time when the MW had been enriched by roughly 10^5 NSMs and 10^8 CCSNe. This makes it difficult to infer which channel is responsible for the majority of r-process production in stars with metallicities close to solar.

This has been the driver behind the trend in recent years to focus high-resolution spectroscopic follow up on low metallicity stars. At [Fe/H] metallicities less than about -2.5, stellar abundances can be interpreted as coming from one or few nucleosynthetic events (Audouze & Silk, 1995; Shigeyama & Tsujimoto, 1998).

One simple way to see this is to note that a single CCSN producing 0.1 $M_\odot$ of Fe sweeps up $\sim 3 \times 10^4$ $M_\odot$ of pristine material by the time its remnant fades into the interstellar medium (Shigeyama & Tsujimoto, 1998), raising the metallicity of the swept material to an [Fe/H] of -2.5.

The focus on observations of r-process elements in low metallicity stars has led to the discovery that the so called main r-process , consisting of elements from Ba to U, seems to follow the same scaled abundance pattern relative to solar across decades in [Fe/H] (Sneden et al., 2008). This implies a mechanism which operates in a robust manner throughout the history of the galaxy and can be explained by extremely neutron rich conditions leading to fission cycling, where nuclei with mass number $A \gtrsim 240$ fission before capturing additional neutrons. The daughter pairs produced then continue to capture neutrons until the relative abundances are in equilibrium determined by beta decay into and out of the isotope. The neutron richness of the material is characterized by the electron fraction Y_e, defined as the number of electrons (or protons) per nucleon in the material, and fission cycling seems to occur efficiently in material with $Y_e < 0.25$ (e.g. Beun et al., 2008).

In addition to this remarkable result, abundance patterns of r-process elements in stars have also shown that the same robustness is not found for elements within the first peak, i.e. from roughly Sr to Ba. Instead, we have observed stars such which show the same robust pattern from Ba to U but a significant scatter in the first peak (Sneden et al., 2008). We have also discovered stars such as HD 122563 which shows significant r-process occuring within the first peak but essentially nothing beyond (Honda et al., 2006). This diversity in the r-process pattern raises the question of whether there are multiple distinct r-process sites, or whether a single site has a very large diversity in nucleosynthetic outcome due to an intrinsic variation in physical parameters. As CCSN simulations have

become more sophisticated, specifically in terms of their neutrino transport, the conditions under which the main / heavy r-process can take place have become more difficult to attain and instead tend to produce mostly first peak elements, which could explain stars such as HD 122563.

More recently, various lines of indirect observational evidence have begun to point toward a progenitor site which operates rarely in comparison to standard CCSNe. One example of this is the discovery of highly r-process enhanced stars in the ultra-faint dwarf (UFD) galaxy Reticulum II (Ji et al., 2016a). At the time, ten UFDs had been observed of which Reticulum II was the only with detections of r-process enhanced stars, immediately implying a rare event. In addition, under conservative estimates of the original gas mass within the galaxy (now depleted), the inferred mass of r-process elements synthesized is consistent with that which NSMs would need to achieve in order to match the average r-process production rate in the MW. This was also consistent with a more recently proposed rare class of magneto-rotational jet driven supernova (Winteler et al., 2012), in which a jet may launch neutron rich material along its poles before significant neutrino irradiation occurs, resulting in an r-process yield similar to NSMs.

1.2.2 Questions Answered and Raised by Direct Observation of an r-process Birthsite

In late 2017 the GW detection of the NSM GW170817 (Abbott et al., 2017b) and subsequent intensive multiwavelength EM observations of AT2017gfo (e.g., Coulter et al., 2017b; Cowperthwaite et al., 2017; Drout et al., 2017b; Shappee et al., 2017) provided indisputable and direct evidence of NSMs being a significant source or r-process elements. This discovery served as a triumph of both observation as well as theory, as the resultant kilonova largely matched theoretical

predictions in terms of its luminosity, color, and evolution (Metzger et al., 2010a; Barnes & Kasen, 2013). One of the interesting aspects of the kilonova was the presence of an early luminous blue component. This component faded within a timescale of days and transitioned into a more slowly evolving red component. This two component behavior was first explained by two geometrically distinct r-process production sites, with the blue being generated at the shock-heated interface of the neutron star surfaces and hydrodynamically squeezed into the polar regions, and the red generated by tidally launched ejecta and a subsequent disk wind (e.g. Kasen et al., 2017a). The inferred masses, coupled with an increasingly secure rate of NSMs in the universe, were able to account for NSMs being the dominant source of r-process creation in the universe.

In the months proceeding the announcement of AT2017gfo, several alternative models emerged regarding the origin of the early blue component. This arose from the tension between the large inferred disk mass, which favors mass ratios far from unity, and the large shock heated mass, which favors equal mass mergers. Some models proposed include shock heating of a cocoon of material expanding around the merger (Piro & Kollmeier, 2018), shock heating of a magnetar wind (Metzger et al., 2018), and a single component model with a time varying opacity (Waxman et al., 2018). As detailed in Arcavi (2018), the early time behavior between a radioactively powered blue component and one arising from shock heating is qualitatively different, and future kilonovae detected within a few hours of a GW trigger will be able to constrain the origin of the blue component.

However the properties of the long lived red component of the kilonova are fully consistent with expectations from the production of a lanthanide-rich ejecta, implicating NSMs as a significant production site of heavy r-process elements. The inferred lanthanide mass fraction of $X_{\mathrm{lan}} \approx 10^{-2}$ implies an abundance distri-

bution which includes all three r-process peaks, possibly consistent with the solar abundance ratios. This raises the question of whether NSMs are able to explain a large majority of r-process production, or if there remains room or necessity for another significant contributor. In addition, at a distance of 40 Mpc, AT2017gfo has only provided evidence of NSMs producing significant r-process in the past 100 Myr. Whether they were also a major progenitor channel at early times remains an open question, and several studies have implicated an alternative early channel based on the chemical evolution trends of Eu and the frequency of low metallicity r-process enhanced stars (e.g. Côté et al., 2018; Safarzadeh et al., 2019). One candidate model recently put forth for this channel is that of a collapsar, in which accretion disk winds from a newly formed black hole may provide the conditions for significant r-process production (Siegel et al., 2019).

Another question trivially raised with a sample size of one is whether AT2017gfo should serve as a standard for typical kilonovae or is drawn from an inherently diverse population, and how diverse that population is expected to be. Several studies have inferred that a diversity is to be expected based on counterpart observations of short gamma-ray bursts (Gompertz et al., 2018; Ascenzi et al., 2019), which is not surprising given the diversity of expected binary parameters such as component masses, spins, and the possibility of a black hole companion. Fully quantifying this diversity will be important for optimizing EM follow-up observation strategies for future events.

Many of these remaining open questions will be answered with GW triggered EM observations of future kilonovae. However given the still uncertain rates and the incredibly difficult task of detecting these counterparts, the timescale on which these questions may be addressed is uncertain. A major effort of my thesis work has been in finding ways to utilize existing stellar abundance data to probe these

questions and make predictions which can be tested against future observations.

1.2.3 Thesis Outline

The outline of the thesis is as follows: In Chapter 2 I describe my contributions to our group's efforts to understand details of the common envelope phase of evolution. In Chapter 3 I describe a method we have developed in order to place stringent constraints on the mass of r-process elements synthesized within a single event in the early universe. In Chapter 4 I present an observational constraint on the viability of the collapsar model as a dominant r-process production site in the early universe. In Chapter 5 I present our predictions for the diversity which may be expected in future kilonovae based on observations of stellar abundances in metal poor stars. In Chapter 6 I briefly discuss ongoing and future work and conclude.

Chapter 2

Common Envelope Evolution as a Precursor to Binary Neutron Stars

2.1 Chapter Abstract

Throughout the course of my PhD I have been involved, at varying levels of contribution as a coauthor, in several projects within the group. These include exploring the dynamics of tidal disruptions of white dwarfs by moderately massive black holes (Law-Smith et al., 2017), investigating fast merging double NS systems in ultra-faint dwarf galaxies (Safarzadeh et al., 2019), examining the role of stellar structure in CE evolution (Everson et al. in prep.), exploring the role of non-solar abundances in SN remnant evolution (Karpov et al. in prep.), using cosmological zoom-in simulations to explore evolution of ^{244}Pu in the solar neighborhood (Ruiz-Rocha et al. in prep.), developing an analytical framework for quantifying the impact of flow morphology in CE events (MacLeod et al., 2017a;

Murguia-Berthier et al., 2017), and modeling a serendipitous stellar merger in M31 (MacLeod et al., 2017b). In this chapter I discuss the last two of these projects where my contributions have had a significant impact on the results obtained. This chapter contains figures and some text from (MacLeod et al., 2017a) and (MacLeod et al., 2017b), with permission, and I only discuss my specific contributions and results within reasonable context.

2.2 An Analytic Plane for Key Common Envelope Flow Parameters

Although the common envelope (CE) evolution plays a critical role in the formation of compact binaries, a deep understanding of the physics governing this process remains elusive due to the large dynamic range in both physical and temporal scales involved (e.g. Ivanova et al., 2013). Our group at UC Santa Cruz has made significant progress in understanding and characterizing the flow close to the embedded object within our "CE Wind Tunnel" (CEWT) framework implemented within FLASH, a three-dimensional adaptive-mesh-refinement hydrodynamics code. The simulation set-up, named the "Common Envelope Wind Tunnel" (CEWT) and initially detailed by MacLeod & Ramirez-Ruiz (2015), is based off of the "wind-tunnel" simulation provided by FLASH in which a constant density and velocity are injected and allowed to interact with a hard shape such as an airfoil. (MacLeod & Ramirez-Ruiz, 2015) significantly expanded upon this by including the effects of gravity from the embedded object, no longer an airfoil but a spherical and accreting boundary simulating an embedded NS.

Quite importantly, the simulation was also augmented to allow for a density gradient to be applied to the inflowing material. This significantly alters the flow
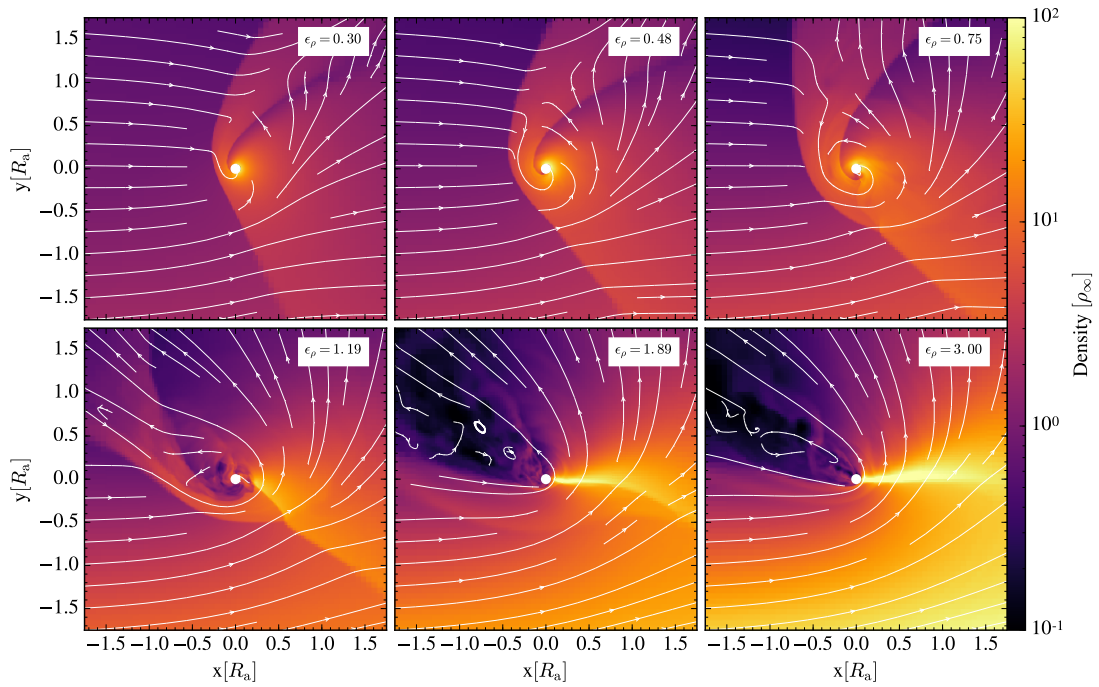
Figure 2.1: Snapshot through the orbital plane of a simulation from (MacLeod et al., 2017a) with $\Gamma_s = \gamma_1 = 5/3$. The density is displayed in color and demonstrates the effect of increasing ϵ_ρ.

morphology resulting from the NS's gravity, transforming it from the well-studied Bondi-Hoyle-Littleton accretion to one in which significant rotation is induced due to the breaking of the symmetry that once caused streamlines to intersect with equal momentum transverse to the embedded object. The resultant flow has a significant effect on both the drag induced onto the NS as well as its accretion rate, greatly suppressing accretion due to an angular momentum barrier and allowing for the NS to end the CE without collapsing to a black hole. Through this study the authors find that the two parameters which govern the flow most strongly are the Mach number $\mathcal{M}$, which affects the strength of the compression post-shock, and the density gradient ϵ_ρ, defined as the number of density scale heights subtended within the characteristic accretion radius of the embedded object. The strength of the density gradient thus quantifies the amount of asymmetry within the initial structure and how much vorticity is induced. Figure 2.1 shows a typical example of the effect of varying ϵ_ρ within this simulation set-up.

This introduces a two-dimensional parameter space of $\mathcal{M}$ and ϵ_ρ to be explored for determining the resultant structures and hence accretion and drag rates within a common envelope encounter. However, this grid must be explored coarsely due to the intensive computational cost of an individual simulation. My specific contribution to this framework has been in reducing the dimensionality of the parameter space by analytically relating the Mach number of the flow to the local density gradient, both of which are extremely important for determining the flow morphology. With a much reduced parameter space, we are now able to perform our simulations in a more targeted and systematic manner. While MacLeod et al. (2017a) goes into much more detail regarding the hydrodynamic simulations and results, I will only describe in this Chapter the derivation of these relations and the applicability to realistic stellar models.

To derive the relationships between the key parameters of common envelope flows, we must first define a few relevant variables. We define our giant primary star to have a mass M_1 and radius R_1, accompanied by a secondary object of mass M_2 and radius R_2, to be embedded within the primary. The separation between the two objects is a, where $a < R_1$ defines the onset of the common envelope. The mass ratio is defined by $q = M_2/M_1$.

The orbital velocity of the secondary is given by

$$v_{\mathrm{k}} = \left(\frac{GM}{a}\right)^{1/2} \tag{2.1}$$

where $M = M_1 + M_2$ is the total mass. Depending on the efficiency of tidal interactions before the encounter, the orbital motion of M_2 is not necessarily expected to be synchronized with the primary's gaseous envelope and the relative velocity is written as $v_\infty = f_{\mathrm{k}} v_{\mathrm{k}}$, where f_{k} is the fraction of keplerian velocity between the secondary object and the gas.

In the cooler outer layers the gas will move supersonically with a Mach number given by

$$\mathcal{M} = \frac{v_\infty}{c_{\mathrm{s},\infty}}. \tag{2.2}$$

Gravitational focussing defines the characteristic accretion radius of the secondary,

$$R_{\mathrm{a}} = \frac{2GM_2}{v_\infty^2}, \tag{2.3}$$

within which the envelope gas will be bound to M_2.

The relationship between R_{a} and a is then given by

$$\frac{R_{\mathrm{a}}}{a} = \frac{2}{f_{\mathrm{k}}^2}\frac{M_2}{M} = \frac{2}{f_{\mathrm{k}}^2}\frac{1}{1 + q^{-1}}. \tag{2.4}$$

This describes the size of the gravitational sphere of influence of the secondary compared to the size of the separation.

A final length scale that plays a critical role in defining the flow morphology is the density scale height,

$$H_\rho = -\left(\frac{d\ln\rho}{dr}\right)^{-1},$$

(2.5)

which is simply the length scale over which the density decreases appreciably. We can then define the ratio

$$\epsilon_\rho = \frac{R_a}{H_\rho}$$

(2.6)

This serves as the measure of the dynamic range in density subtended within the sphere of influence of the secondary and governs the amount of rotation induced within the flow.

With these quantities defined, we can derive the relationships between flow parameters.

We begin with the hydrostatic equilibrium of the primary's envelope,

$$\frac{dP}{dr} = -g\rho.$$

(2.7)

We re-write the left-hand side as $dP/dr = (dP/d\rho) \times (d\rho/dr)$. We can then use the derivative of pressure with respect to density within the envelope to find,

$$\frac{dP}{d\rho} = \Gamma_s \frac{P}{\rho} = \gamma_1 \left(\frac{\Gamma_s}{\gamma_1}\right)\frac{P}{\rho} = \left(\frac{\Gamma_s}{\gamma_1}\right)c_s^2,$$

(2.8)

where here we denote

$$\left(\frac{d\ln P}{d\ln \rho}\right)_{\text{envelope}} = \Gamma_{\text{s}}, \tag{2.9}$$

as the polytropic index of the stellar structure, which is not necessarily identical to the adiabatic index

$$\left(\frac{d\ln P}{d\ln \rho}\right)_{\text{ad}} = \gamma_1. \tag{2.10}$$

For example, the atmosphere of the earth close to the surface is well described by a constant temperature, i.e. $\Gamma_{\text{s}} = 1$. However a parcel of ideal atmosphere which is compressed adiabatically will in response behave with $\gamma_1 = 5/3$. This response index is that in which the square of the sound speed $c_s^2 = \gamma_1 P/\rho$. We note that in a region of efficient convection within a star, $\gamma_1 = \Gamma_{\text{s}}$. It is also useful to define

$$\left(\frac{d\ln T}{d\ln \rho}\right)_{\text{ad}} = \gamma_3 - 1, \tag{2.11}$$

which enters into the equation of state relating pressure, density and internal energy as $P = (\gamma_3 - 1)\, ne$. Deviations from $\gamma_1 = \gamma_3$ may arise from contributions to the internal energy due to radiation pressure, as an example.

Substituting Equation (2.9) in, our expression becomes,

$$\frac{c_s^2}{\rho}\frac{d\rho}{dr} = -g\left(\frac{\Gamma_{\text{s}}}{\gamma_1}\right)^{-1}. \tag{2.12}$$

We substitute in the definition of the density scale height (equation 2.5), the definition of g, and set $r = a$ (the separation of the pair) to find

$$\frac{c_s^2}{H_\rho} = \frac{GM_1}{a^2}\left(\frac{\Gamma_{\text{s}}}{\gamma_1}\right)^{-1}. \tag{2.13}$$

We use the definition of v_{k}, equation (2.1), and total system mass $M = M_1 + M_2$

to write

$$c_s^2 H_\rho^{-1} = \frac{v_k^2}{a} \frac{M_1}{M} \left(\frac{\Gamma_s}{\gamma_1}\right)^{-1}. \tag{2.14}$$

Then, rearranging and introducing the Mach number, equation (2.2), based on a flow relative velocity $v_\infty = f_k v_k$,

$$\frac{a}{H_\rho} = \frac{v_k^2}{c_s^2} \frac{M_1}{M} \left(\frac{\Gamma_s}{\gamma_1}\right)^{-1} = \frac{\mathcal{M}^2}{f_k^2} \frac{M_1}{M} \left(\frac{\Gamma_s}{\gamma_1}\right)^{-1}. \tag{2.15}$$

We can then substitute in for the accretion radius R_a and ϵ_ρ, equations (2.3) and (2.6), to express the relationships between the flow parameters,

$$\mathcal{M}^2 = \epsilon_\rho \frac{(1+q)^2}{2q} f_k^4 \left(\frac{\Gamma_s}{\gamma_1}\right) \tag{2.16}$$

or

$$\epsilon_\rho = \frac{2q}{(1+q)^2} \mathcal{M}^2 f_k^{-4} \left(\frac{\Gamma_s}{\gamma_1}\right)^{-1}. \tag{2.17}$$

These equations relate the key quantities in dictating flow morphology of the common envelope interaction and thus allow us to explore the parameter space of physically realizable scenarios in a targeted way.

Figure 2.2 shows examples of two stellar profiles computed using the `MESA` stellar evolution code version 8845 (Paxton et al., 2011, 2013, 2015), of which the details can be found in MacLeod et al. (2017a). As can be seen in the lower panel, we find good agreement between our equations and the profiles, indicating that the Mach number of the flow and the local density gradient are indeed related to eachother, even in the interiors of very different stars.
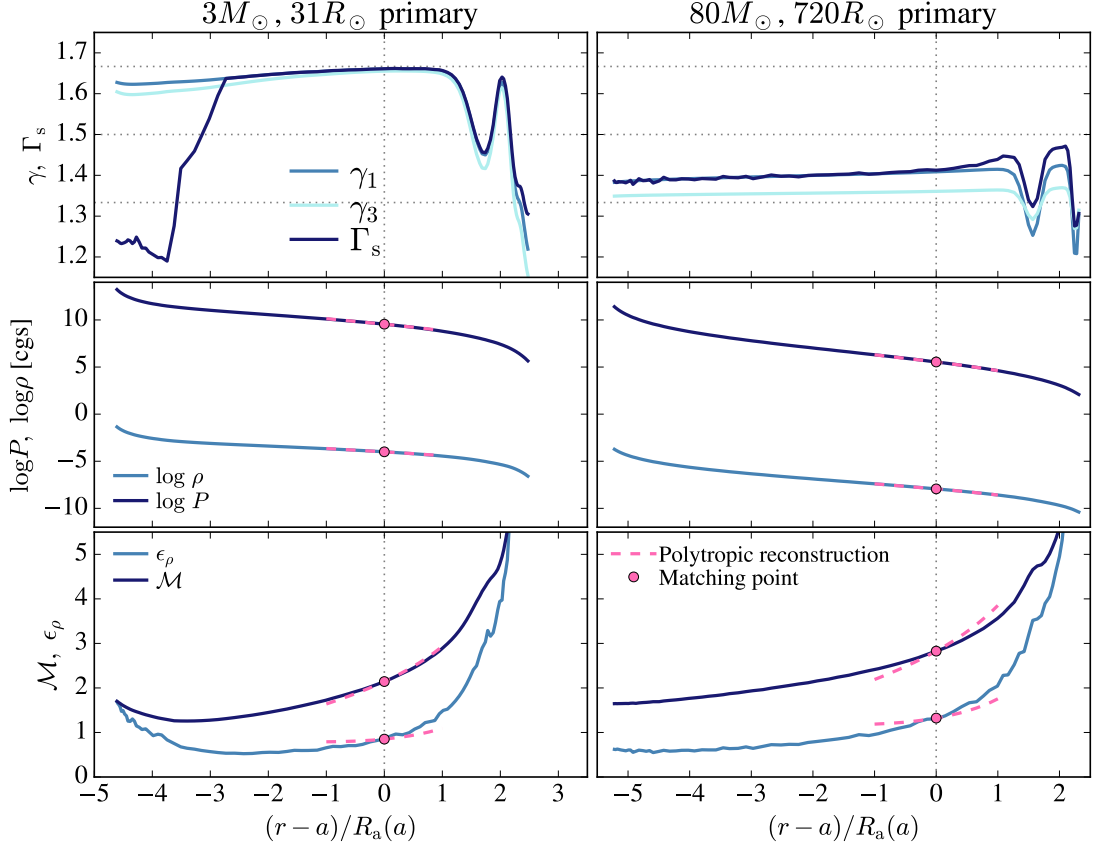
Figure 2.2: Profiles of primary-star stellar structure relevant to common envelope inspiral from MacLeod et al. (2017a). A secondary star is embedded within the envelope of the primary at the separation marked with the vertical line. The x-axis shows radial distance in units of the accretion radius, R_a. The top panel compares profiles of gas adiabatic exponents, γ_1 and γ_3, along with the local structural parameter Γ_s. Note that γ_1 and γ_3 are relatively similar to each other, and additionally, that in convective regions of the stellar envelopes $\gamma_1 \approx \Gamma_s$. The center panel shows profiles of density and pressure, with local polytropic reconstructions extending $\pm R_a$ (pink dashed lines). The lower panel shows that these properties can be matched to a flow Mach number, $\mathcal{M}$ and density gradient ϵ_ρ, at the position of the embedded object. The slope of the polytropic profile of these secondary parameters is approximate but not perfectly fit, however, as can be seen in the lower panel.

2.3 Lessons from the Onset of a Common Envelope Episode: the Remarkable M31 2015 Luminous Red Nova Outburst

In addition to simulations of the onset of the common envelope (e.g. MacLeod et al., 2018), observations have been able to place constraints on the conditions at the onset of a CE event through luminous red novae (LRN). These are thought to come from low mass stellar mergers which result in ~ 100 day transients which significantly redden over time. The best studied LRN is V1309 Scorpii, where pre-merger photometry of the progenitor was taken over several years by the Optical Gravitational Lensing Expirement (Rucinski, 1998) and was consistent with a W Uma type overcontact binary with an exponentially decreasing orbital period. Following the merger, the periodicity induced by the peanut shape of the overcontact binary disappeared, indicating the presence of only a single object which became increasingly red and enshrouded in dust (Tylenda et al., 2011; Nicholls et al., 2013).

This pointed directly to a merger of two low mass stars (Tylenda et al., 2011) and shed light on the conditions which may have led to the merger. One way in which a system may be driven to merge is through the Darwin Instability (Darwin, 1879), in which the orbital angular momentum budget of the binary is no longer sufficient to maintain synchronicity of the components through tides. This leads to an continuously decreasing orbital period as observed in V1309 Sco, resulting in the merger of the binary components.

Serendipitously, a LRN (M31LRN 2015) was detected in the Andromeda galaxy in January 2015 (Williams et al., 2015; Kurtenkov et al., 2015). The source was detected in the B,V,R, and I bands, reaching a peak magnitude of roughly -9 in

all bands and fading and reddening over 50 days. While we were not fortunate enough to have time-series photometry as in the case of V1309 Sco, a progenitor system consistent with the position of the LRN was detected with the *Hubble Space Telescope* (HST) in August of 2004. Because of the known distance to the source, we are able to calculate the absolute magnitude and color of the progenitor subject to reddening uncertainty. For a reddening toward the source of $E(B-V) = 0.12 \pm 0.06$ mag (Williams et al., 2015), we transform the HST detections to calculate $M_V = -1.50 \pm 0.23$ mag, and $(V-I) = 1.05 \pm 0.15$ mag. However, the reddening is reported as $E(B-V) = 0.35 \pm 0.1$ mag by Kurtenkov et al. (2015). To account for these uncertainties in our modeling of the progenitor, we take the full range of reddening values into account, i.e. $E(B-V)$ between 0.05 and 0.45 mag.

My specific contribution to this project was in calculating stellar models in order to match the observed progenitor properties and aiding in the interpretation. MacLeod et al. (2017b) explores in greater detail the transient event itself in order to derive constraints on the nature of the outburst, however here I focus on the immediate implications of the pre-outburst source.

To map the pre-outburst HST color and magnitude to the properties of a progenitor star we compute a grid of stellar models with the `MESA` stellar evolution code version 7624 (Paxton et al., 2011, 2013, 2015). We assume that the light at this time is dominated by the primary star and thus calculate single stellar models. We compute stellar tracks for stars of solar metallicity with masses between 2 and 8 $M_\odot$ from the pre main sequence until core helium ignition.

We use a modified version of the input lists provided to recreate Figure 16 of Paxton et al. (2013) which are available on `mesastar.org`. The initial models have a composition of $Y = 0.272$ and $Z = 0.02$ and convection is determined by

the Schwarzschild criterion using $\alpha_{\mathrm{MLT}} = 2$ and allows for exponential overshoot by 1% of the scale height (`overshoot_f`= 0.014 and `overshoot_f0`= 0.004). We include mass loss along the RGB through a Reimers (1975) wind prescription with $\eta_{\mathrm{R}} = 0.5$ and do not include the effects of rotation. We calculate nuclear reactions using the JINA reaclib rates (Cyburt et al., 2010). We use standard OPAL opacities (Iglesias & Rogers, 1996) and we calculate surface properties using a grey atmosphere approximation. To map the MESA variables to a color and magnitude we use the MESA colors package, which follows the method outlined in Lejeune et al. (1997, 1998) to yield $UBVRI$ colors given surface temperature, surface gravity, and metallicity.

Figure 2.3 shows how our stellar models traverse through the color-magnitude diagram and intersect the HST observations. We find the models to be consistent with a 3-5 $M_{\odot}$ subgiant in the process of expanding, lending credence to our simplified single star modeling. With this validation, we are able to probe deeper questions regarding the onset of M31LRN 2015. Because the MESA models provide the full structural profile of the progenitor star, we can infer properties in addition to the mass which inform our understanding of this event.

Figure 2.4 shows the evolution of several key physical quantities in our models. They predict a star which is undergoing expansion and has grown to a size of 35-40 $R_{\odot}$, which can be inferred as being comparable to the separation of the binary at the time of merger. We also infer, given the masses and radii of our models, an escape velocity of 200-350 km s^{-1}, consistent with the velocity inferred through Hα measurements of 370 ± 240 km s^{-1} taken 4.7 days prior to peak (Williams et al., 2015). Finally, we see that as the star begins to make its way toward the giant branch and the envelope transitions from radiative to convective, the specific moment of inertia, where we calculate the moment of inertia as
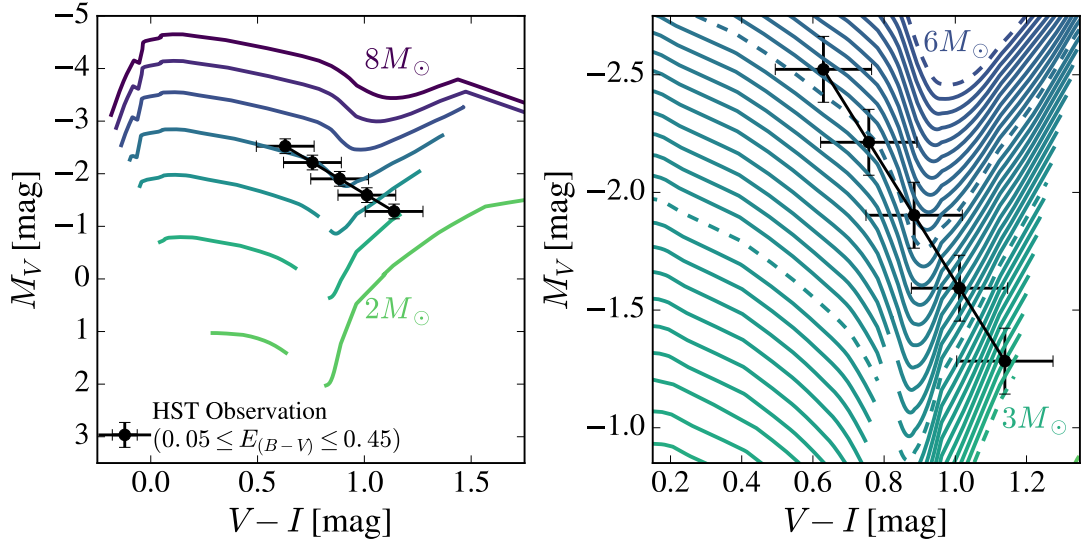
Figure 2.3: `MESA` stellar evolutionary tracks through the color-magnitude diagram used to infer properties of the progenitor system for M31LRN 2015. The HST detections are shown as points for individual reddening estimates of $E(B-V)$ between 0.05 and 0.45 in intervals of 0.1 mag. Error bars show distance and measurement error, but not reddening. The left panel shows our initial range of 2 to 8 $M_\odot$ models. The right panel shows a zoom in of the region subtended by the observations, and consists of models between 3 and 6 $M_\odot$ in intervals of 0.1 $M_\odot$ with integer values indicated by a dashed line. We mask the portions of the tracks in which the stellar radius is decreasing as the merger should be triggered by the expansion of the primary star. The HST measurements seem to implicate an expanding subgiant star of 3-5 $M_\odot$.
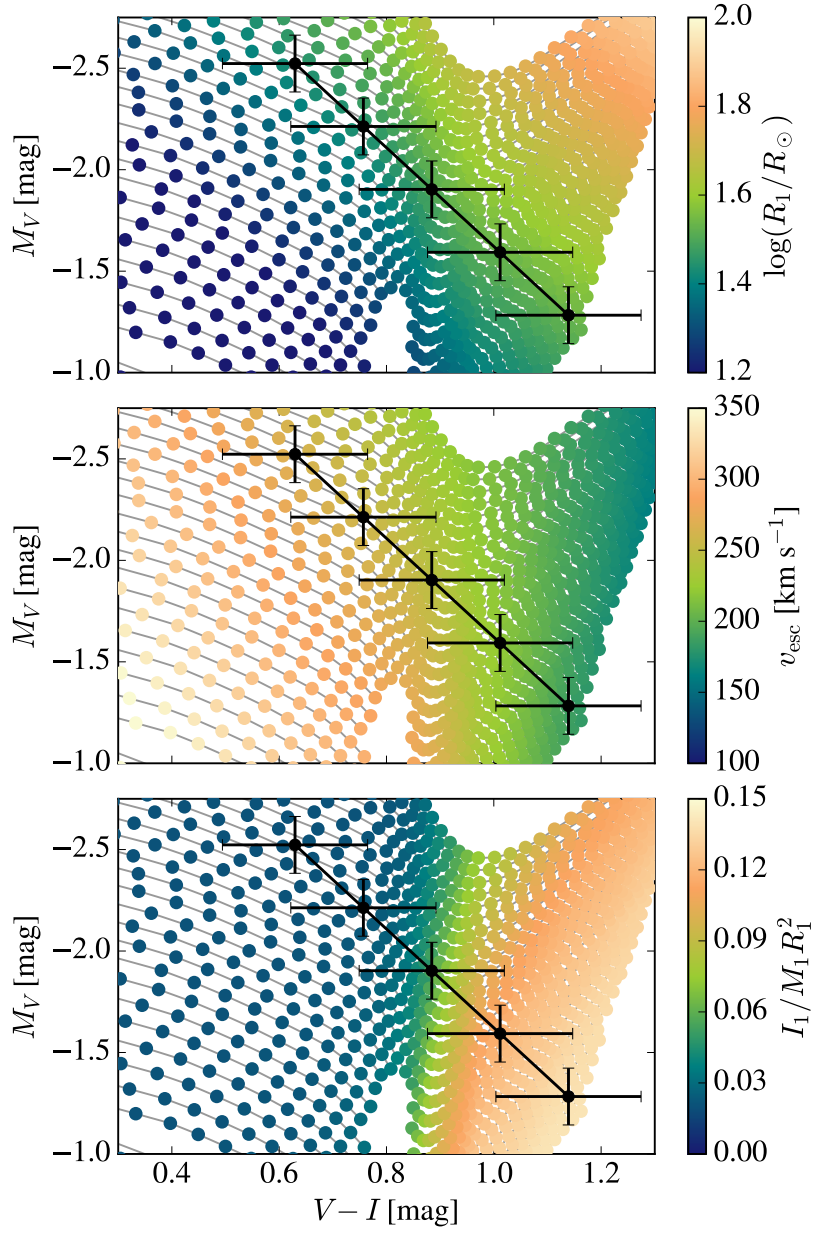
Figure 2.4: `MESA` stellar evolutionary tracks through the color-magnitude diagram, here in color showing key physical quantities related to a stellar merger. The upper panel shows that the models are all undergoing radial expansion at the time they cross the locus of observational constraints. The center panel shows the escape velocity from the surface of the primary. The lower panel shows the growth of the specific moment of inertia due to the transition from a radiative to a convective envelope.

$$I_1 = \frac{8}{3}\pi \int_0^{R_1} \rho_1(r) r^4 dr, \qquad (2.18)$$

begins to increase due to the presence of more mass in its outer layers. This will cause the primary star to be more difficult to synchronize with the orbital frequency, perhaps initiating the Darwin instability and leading to the merger 10 years later.

As mentioned previously, MacLeod et al. (2017b) derive many more constraints on this remarkable transient, but my efforts within this work were focussed on what we can learn based on modeling of the progenitor system pre-outburst. Through stellar evolution modeling of the source, we are able to gain insight into the potential well in which the event took place, to probe possible reasons leading to the merger, and to infer the presence of dynamical ejecta launched near the escape velocity.

2.3.1 A Brief Aside

While exploring the intricacies associated with the formation of these compact binaries, I developed a deep interest in understanding the eventual fate of these systems. Fortunately, our group was and continues to be actively interested in this exact topic, and on one fateful day I accidentally walked into a meeting where r-process nucleosynthesis was the topic of discussion. This immediately piqued my interest, and the remaining Chapters of my thesis represent my foray into this field. Pardon the jump cut.

Chapter 3

A Stringent Limit on the Mass Production Rate of r-process Elements in the Milky Way

3.1 Chapter Abstract

We analyze data from several studies of metal-poor stars in the Milky Way, focusing individually on main r-process elements (Eu) as well as the lighter neutron-capture element Sr, at the neutron-magic peak N=50. Because these elements were injected in an explosion, we calculate the mass swept up when the blast wave first becomes radiative, yielding a lower limit for the dilution of such elements and hence a lower limit on the ejecta mass that is incorporated into the next generation of stars. Our study demonstrates that in order to explain the largest enhancements in [Eu/Fe] observed in stars at low [Fe/H] metallicities, individual r-process production events must synthesize a minimum of roughly 10^{-3} $M_\odot$ of r-process material. This provides a critical constraint on galactic chemical evolution

models. We also show independently that if the site of Mg production is the same as that of Eu, individual injection events must synthesize up to $\sim 10^{-3}$ $M_\odot$ of r-process material. On the other hand, demanding that Sr traces Mg production results in r-process masses per event of $\sim 10^{-5}$ $M_\odot$. This suggests that the astrophysical sites responsible for the genesis of the main r-process elements need to operate at a drastically reduced rate when compared to standard core-collapse supernovae.

3.2   Introduction

Although the physical conditions required for r-process nucleosynthesis to occur have been understood since Burbidge et al. (1957) and Cameron (1957), the astrophysical site(s) in which those conditions are realized remains unclear [1]. Whether enrichment has occured via Type II Supernovae (SNe, e.g. Woosley et al., 1994), in which the injection in a galaxy occurs frequently ($\sim 10^{-2}$ yr^{-1}) with low ($\sim 10^{-5}$ $M_\odot$) masses, or through sporadic ($\sim 10^{-5}$ yr^{-1}) injection by neutron star mergers (NSM, e.g. Lattimer & Schramm, 1974a) of high ($\sim 10^{-2}$ $M_\odot$) masses is difficult to discern at high metallicities, as any hysteresis has been eradicated by multiple enrichment events.

For this reason, metal-poor stars in the galactic halo serve as laboratories for the study of r-process element synthesis and can shed light on the identity of their progenitors (Sneden et al., 2008). Abundance comparisons between many metal-poor halo stars suggest that the r-process mechanism is rather robust. In other words, we see the same relative proportions of r-process elements in stars that are many billions of years different in age, indicating that this process has

---

[1]This work was first submitted prior to the detection of the binary neutron star merger GW170817 / SSS17a (Abbott et al., 2017b; Coulter et al., 2017b).

operated in a fairly consistent manner in the history of the Galaxy. This result provides critical information regarding the specific physical conditions resulting in the nuclear pathways required for the r-process.

In the metallicity range [Fe/H] of roughly -2 to -3.5, where we are using the standard notation $[X/H] = \log_{10}(X/H) - \log_{10}(X/H)_\odot$, r-process elements have been found to exhibit large star-to-star bulk scatter in their concentrations with respect to the lighter elements, but with a distribution that is characteristic of solar system matter. This hints at the presence of chemically inhomogeneous and unmixed gas at that epoch (Fields et al., 2002). As time evolves, these localized inhomogeneities are smoothed out as more events occur and r-process products migrate and mix throughout the Galaxy. Recently, "zoom-in" cosmological simulations of heavy element production in a Milky Way-like (MW-like) galaxy have shown the observed stellar abundances resulting from this process to be consistent with NSMs being the dominant enrichment mechanism (Shen et al., 2015; van de Voort et al., 2015; Naiman et al., 2018), but must rely on prescriptions regarding how material is mixed in the young MW and suffer from uncertainties in the delay time for NSMs.

In this paper we use simple and conservative physical arguments to show that to show that the scatter in Eu and lighter neutron-capture elements such as Sr at low [Fe/H] metallicities can be used to place stringent lower limits on how much r-process material needs to be synthesized per injection event in the early Universe. In Section 3.3 we combine abundance data from several previous studies of MW stars and focus on Mg production to identify stars that may have formed from gas that has been enriched by no more than a few nucleosynthetic events. In Section 3.4 we derive lower limits on the r-process production required to explain Eu enhancements in these same stars, and also demonstrate the implications of

demanding that r-process enhancements trace the Mg source. In Section 5.5 we discuss our findings and explore the possibility of distinguishing between rare events by considering the environment in which they may take place.

3.3 Supernova II as Testbeds for Metal Enrichment

While there is no current consensus on the dominant channel of r-process production, it is well understood that the so-called α (O, Mg, Si, Ca, and Ti) elements are primarily produced in massive stars and returned to the interstellar medium (ISM) via core-collapse SNe (Burbidge et al., 1957; Woosley & Weaver, 1995). For this reason, elements such as Mg have been measured in metal-poor MW halo stars to study the efficiency of galactic mixing in the early universe (Arnone et al., 2005). Here we focus on Mg production in the MW in order to demonstrate how our physical argument applies to a relatively well-understood production source.

SNe input approximately 10^{51} erg of energy into their surroundings, resulting in a blast wave that sweeps up a less α-enhanced ISM, thereby mixing and diluting any enhancement supplied by the ejecta. In order to incorporate these metals into a new generation of stars the SN blast wave must first cool, at the very least. The mass swept up before the blast wave becomes radiative and cools efficiently in a homogeneous medium is given by

$$M_{\text{cool}} \approx 10^3 \left(\frac{Z}{Z_\odot} \right)^{-3/7} \left(\frac{n_{\text{ISM}}}{10^2 \, \text{cm}^{-3}} \right)^{-2/7} \left(\frac{E_{\text{exp}}}{10^{51} \text{erg}} \right)^{6/7} M_\odot, \qquad (3.1)$$

where E_{exp} is the explosion energy, and Z and n_{ISM} are the metallicity and number density of the surrounding ISM, respectively (Cioffi et al., 1988; Thornton et al.,

1998; Martizzi et al., 2015). For a given ejecta mass, the maximum enhancement possible of the surrounding ISM (to be observed in the next generation of stars) occurs when the ejecta has mixed with M_{cool}, as further mixing (which inevitably occurs due to the inertia of the expanding material as well as larger-scale mixing due to, e.g., turbulence generated by galactic shear) will further dilute the enhancement (Greif et al., 2009).

One can then invert this relation to find the minimum mass of the event for a given enhancement in the next generation of stars, which is given by

$$M_X \geq X_\odot \times 10^{\,[\mathrm{X/H}]} \, M_{\mathrm{cool}}, \tag{3.2}$$

where $X_\odot$ is the mass fraction of element X within the Sun. This is the mass required to explain a given stellar enhancement, assuming the ejecta is only mixed within a cooling mass. Since the ejecta certainly mixes with greater than a cooling mass and further dilutes, Equation (3.2) represents a strict lower limit for low-metallicity stars that have not been enriched by multiple events. Recent hydrodynamical simulations show final swept-up masses between 1700 $M_\odot$ in a homogeneous ISM and 8000 $M_\odot$ in a turbulent ISM with similar scalings, indicating that our analytical estimate is conservative (Martizzi et al., 2015).

In Figure 3.1 we plot [Mg/Fe] as a function of [Fe/H] for a compilation of MW stars and show in color the minimum M_{Mg} required to explain the observations, assuming that the ISM that collapsed to form the stars was enhanced by a single event that input 10^{51} ergs of energy. This simplistic assumption clearly breaks down at high metallicities where the gas has been enhanced by many events in the history of the galaxy, but we note some interesting behavior at low metallicity. First, at [Fe/H] $\lesssim$ -2.5, the stars are all consistent with a minimum Mg mass lower than 0.1 $M_\odot$, which is shown by the dashed line and is roughly in agreement with
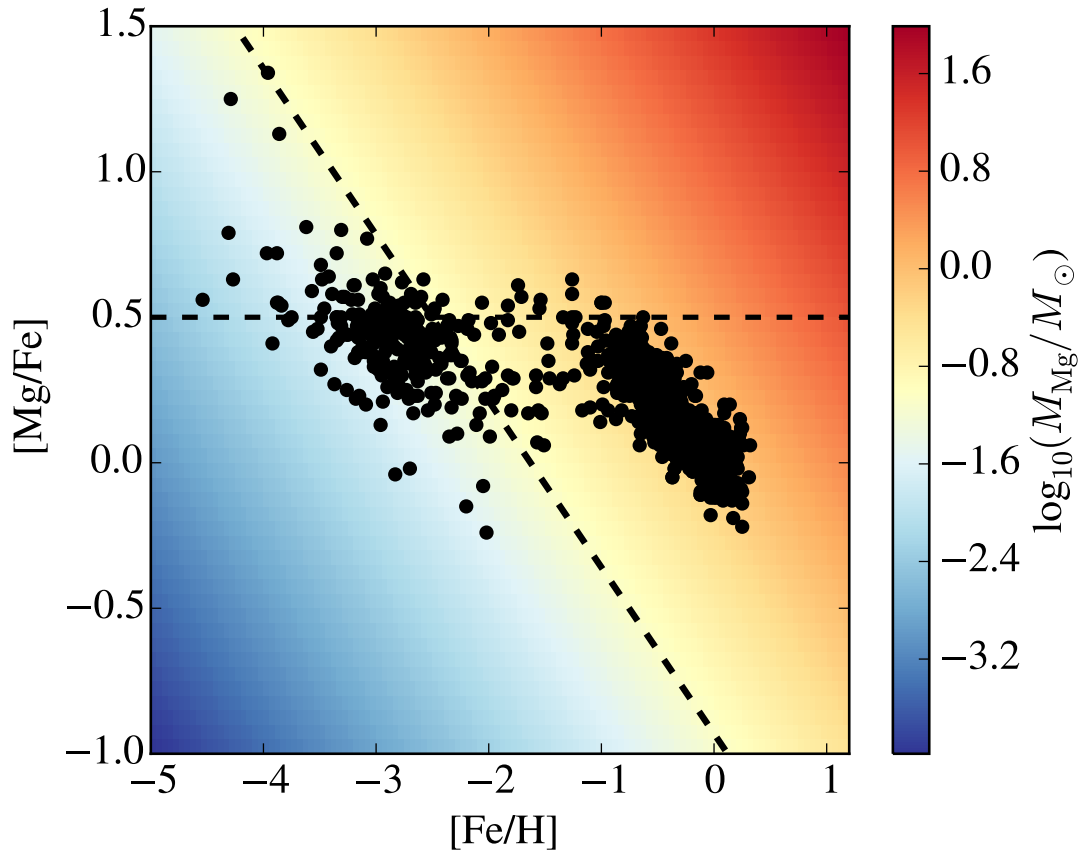
Figure 3.1: Mg abundance as a function of metallicity for our total star sample. We show abundance data from Roederer et al. (2014), Reddy et al. (2006), Reddy et al. (2003), Cayrel et al. (2004), Venn et al. (2004), Barklem et al. (2005) and Fulbright et al. (2010) with black dots. The mass of Mg required to explain the abundances if the ejecta is mixed over one cooling mass is shown in color (see text). The diagonal line represents a Mg mass of 0.1 $M_\odot$, and the horizontal line represents the IMF and metallicity-weighted yield for SN ejecta.

the Mg mass expected to be produced in a single, standard core-collapse SN (Kobayashi et al., 2006; Nomoto et al., 2006). We do not expect a clustering at exactly the dotted line as the SNe likely mix well past their cooling mass, resulting in a vertically downward trajectory in the plot. At higher metallicities, we see a convergence toward [Mg/Fe] = 0.5, which is roughly the IMF-weighted yield of SN ejecta (e.g., Kobayashi et al., 2006). At this point, the gas is well mixed and is clearly incompatible with pollution by a single event, as further evidenced by the high masses required to explain the enhancement.

The dearth of stars in the upper right quadrant is easy to understand. At the lowest metallicities, star forming gas is unlikely to have been polluted by more than the mass of a single event (shown by the diagonal dashed line), while at higher metallicities, it is impossible to enrich beyond the yields since the mass fraction is an intensive quantity, i.e. the enrichment has converged to the yields.

Because we wish to constrain the mass per event of r-process material, we do not consider this integrated history and instead focus our attention on metallicities lower than that in which the enriched gas has reached [Mg/Fe] abundance ratios close to those given by SN yields ([Fe/H] < -2.5).

3.4   Constraints on r-process Production

3.4.1   A Strict Lower Limit

With the data set now consisting of only these low-metallicity single event candidates, we can begin to ask more probing questions. First, we can repeat exactly the same exercise that we did as for Mg on a so-called r-process-only element, Eu, for the same set of stars. At these low metallicities, heavier elements such as Eu certainly cannot have saturated to the yields, as the overall mass
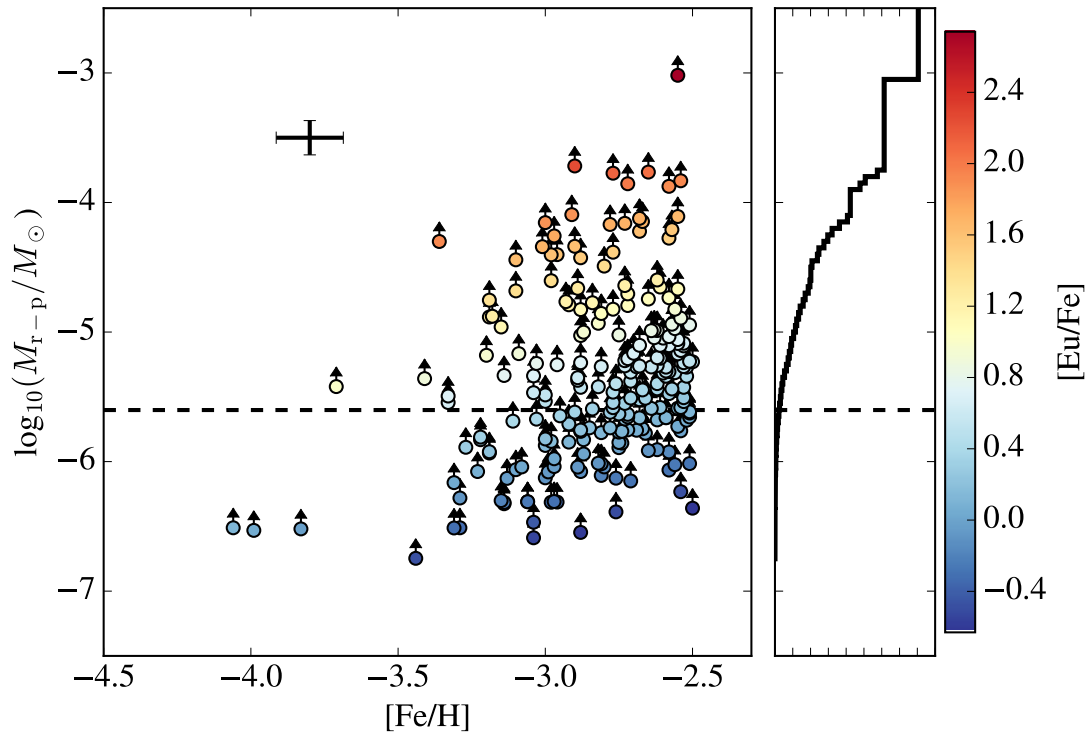
Figure 3.2: Inferred minimum *r*-process mass per event as a function of metallicity with a mass-weighted cumulative histogram in projection. Color marks the observed [Eu/Fe] for these stars, and the size of the average error bar is shown in the top left corner.

production rate of Mg exceeds that of Eu by several orders of magnitude. Because the main r-process pattern has been shown to be robust, we can then scale the Eu mass to a total r-process mass within the second and third peaks demanded by the Eu abundances.

For these scalings, we use a total solar r-process mass fraction of $X_{\text{r-p},\odot} = 3.5 \times 10^{-7}$ (with 3.6×10^{-10} in Eu) , which is composed of 78% light (first peak) and 22% in the main component (Arnould et al., 2007). We distinguish the boundary between light and main at a mass number A of 90. This analysis does not depend on the initial ejecta configuration (e.g. spherical ejecta as opposed to tidal tails), as the initial conditions are quickly forgotten and the explosion finds the standard, spherical Sedov–Taylor blast wave solution long before reaching the cooling radius (Montes et al., 2016).

We assume a total r-process mass production rate of $\dot{M}_{\text{r-p}} \approx 10^{-7}\ M_\odot\,\text{yr}^{-1}$, which is consistent with observations (Cowan & Thielemann, 2004; Sneden et al., 2008). For a SN rate of $10^{-2}\ \text{yr}^{-1}$, the mass per event required to be consistent with $\dot{M}_{\text{r-p}}$ is $7.8 \times 10^{-6}\ M_\odot$ for the first peak, $2.2 \times 10^{-6}\ M_\odot$ for the main component, and thus $10^{-5}\ M_\odot$ in total.

For a current compilation of heavy element measurements in low-metallicity stars, we utilize the SAGA database (Suda et al., 2008), which compiles literature results and ensures consistency in, e.g., solar abundance values. Figure 3.2 shows the result of this experiment. We find that if the events that caused the Eu enhancement formed the next generation of stars at the cooling mass of the blast wave, these events would correspond to a total r-process mass of up to $10^{-3}\ M_\odot$. We emphasize that each one of these points is a minimum mass per event, and thus represent lower limits. Most of our data are inconsistent with the 2.2×10^{-6} $M_\odot$ per event (shown by the horizontal dashed line) necessary to produce the total

main r-process content in the Galaxy given an average SN rate of 10^{-2} yr^{-1}.

The mass-weighted, cumulative histogram shown in projection at the right can be read as stating that although a significant fraction of stars do not contradict a production rate of 10^{-2} yr^{-1} or more, essentially all of the mass production must come from less frequent events.

We can perform this same experiment on Sr, a lower mass element that may be produced in a less neutron-rich environment, e.g. a neutrino-driven wind (e.g., Arcones & Montes, 2011), in order to infer upper limits on the event / injection rate of the lighter first-peak r-process elements. Figure 3.3 shows the result of this experiment. Unlike Eu, we find that Sr is marginally consistent with a mass per event of $\lesssim 7.8 \times 10^{-6}$ $M_\odot$, resulting in an average injection rate of $\gtrsim 10^{-2}$ yr^{-1}. This implies that standard CCSNe are consistent with being a significant source of first-peak r-process material given their rate, in contrast to our Eu findings. However, we note that several stars, and roughly half of the total inferred mass, are inconsistent with this rate. Again, considering that these inferred masses can only move upward under our assumptions, this may imply large variations from event to event, or multiple progenitor channels. Recently, several studies have indicated that there may be multiple sites for the first peak, which these discrepancies may also be pointing toward.

3.4.2 Constraints Based on Mg Mixing

We now return our attention to our original sample of stars with Mg and Eu measurements from Section 3.3 and attempt to place constraints under the assumption of the Mg and r-process elements coming from the same source. Numerical simulations of SN nucleosynthesis have provided us with the average amount of Mg mass ejected in SNe across a wide range of progenitor masses and metal-
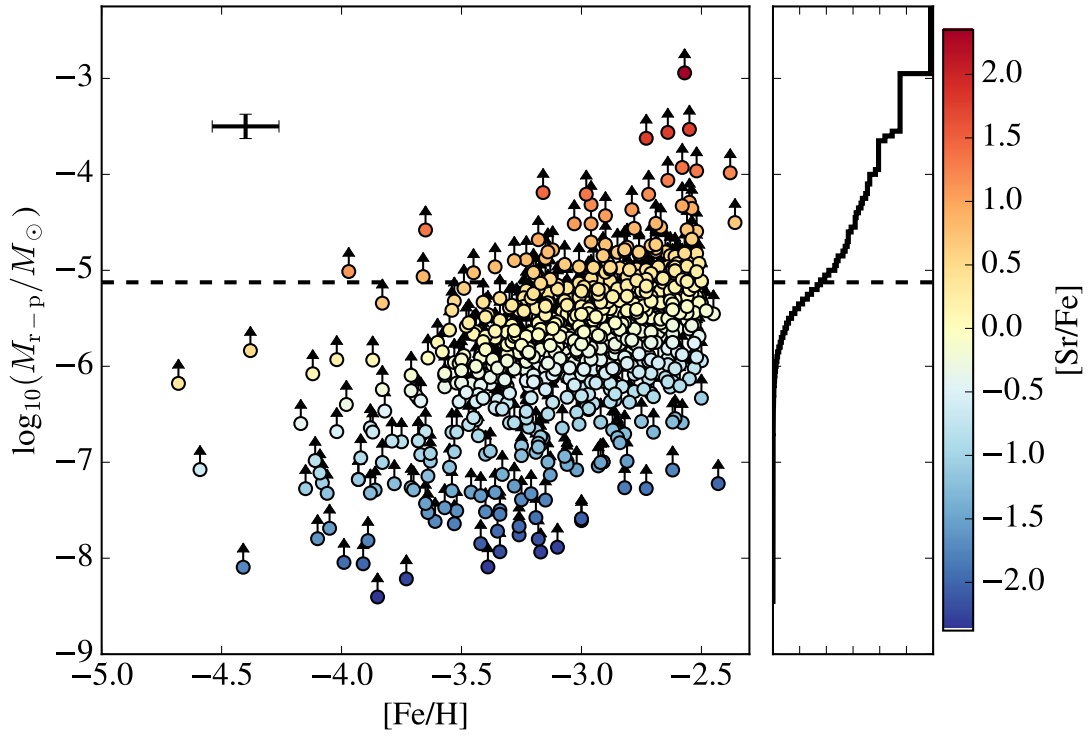
Figure 3.3: Inferred lower limit on Sr ejecta mass based on M_{cool}. This first-peak r-process element is consistent with a mass per event of roughly 7.8×10^{-6} $M_\odot$ of first-peak r-process ejecta, which is consistent with an injection rate of 10^{-2}yr^{-1}

licities (e.g., Kobayashi et al., 2006). Similar to Fields et al. (2002), with these results we can calculate the mixing mass (denoted here as M_{mix}), i.e., the ISM mass over which the Mg must be diluted in order to explain the observed stellar abundances if the subsequent generation of stars were formed by gas that was enriched by a single pollution event,

$$M_{\mathrm{mix}} = 130 \times 10^{-[\mathrm{Mg/H}]} \left(\frac{M_{\mathrm{Mg}}}{0.1\,M_\odot} \right)\,M_\odot, \tag{3.3}$$

where we have used $X_{\mathrm{Mg},\odot} = 7.2 \times 10^{-4}$ (Lodders, 2003) and a fiducial SN Mg mass of 0.1 $M_\odot$. The normalization for the mixing mass is not to be taken at face value since the galaxy is well mixed in α elements at [Mg/H] = 0. Figure 3.4 shows our reduced sample, now in color showing M_{mix} for a fiducial SN Mg mass of 0.1 $M_\odot$. We can then use the ansatz that the source of the Mg is the same as that of both Eu and Sr. As mentioned before, Sr (unlike Eu) may be synthesized in a less neutron-rich environment, which is realized in either SNe, NSMs, or both. At these low metallicities, we do not consider the s-process from asymptotic giant branch stars to contribute to the observed Sr abundances, although massive low-metallicity rotating stars may contribute to a primary s-process (Pignatari et al., 2008; Frischknecht et al., 2016). While our findings could in principle be used to place constraints on the production efficiency of this channel at low metallicities, we do not attempt this exercise here.

If these elements are coming from the same astrophysical site, this mixing mass should be the same for Eu and Sr as for Mg, allowing us to infer a total r-process mass per event. With this assumption, we can perform the same exercise as before, now replacing the cooling mass with the mixing mass as our reference mass scale. If the source of Mg is responsible for creating the entirety of the r-process elements, we can again convert from an elemental mass to total r-process

mass by scaling the relative abundances to match the solar values, i.e.,

$$M_{\text{r-p}} = X_{\text{r-p},\odot} \times 10^{\,[\text{Eu/H}]} M_{\text{mix}}. \tag{3.4}$$

However, if the Mg source is only responsible for the lighter, first-peak elements, we have instead

$$M_{\text{r-p}}^{\text{l}} = f_{\text{l}} X_{\text{r-p},\odot} \times 10^{\,[\text{Sr/H}]} M_{\text{mix}}, \tag{3.5}$$

where we use $X_{\text{r-p},\odot} = 3.5 \times 10^{-7}$, and f_{l} is the fraction of total r-process mass in the light r-process element ranges, as defined in Section 3.1.

Mixing is element agnostic, so we can test the consequences of this hypothesis and answer the question of r-process production required by SN in order to explain the observed abundances at low metallicities. Figure 3.5 shows the results. For Sr, demanding that the source of Mg production in the early universe also produces the first r-process peak elements results in masses well above the 7.8×10^{-6} required to have the mass per event consistent with an average SN rate of 10^{-2} yr^{-1}.

These results may be of particular interest, as first-peak r-process elements have been successfully synthesized in SN nucleosynthesis calculations for some time as well as in recent NSM simulations (Martin et al., 2015; Wu et al., 2016a). In the NSM case, the main r-process elements are robustly synthesized in the initial dynamical ejecta. However, a remnant accretion disk around a hyper-massive neutron star (HMNS) or black hole may provide the conditions for creation of the first-peak elements. The mass of this component remains uncertain to within orders of magnitude and is very sensitive to several parameters, e.g. the lifetime of the HMNS.

For Eu, we wish to test a Mg source that would also create all r-process peaks,
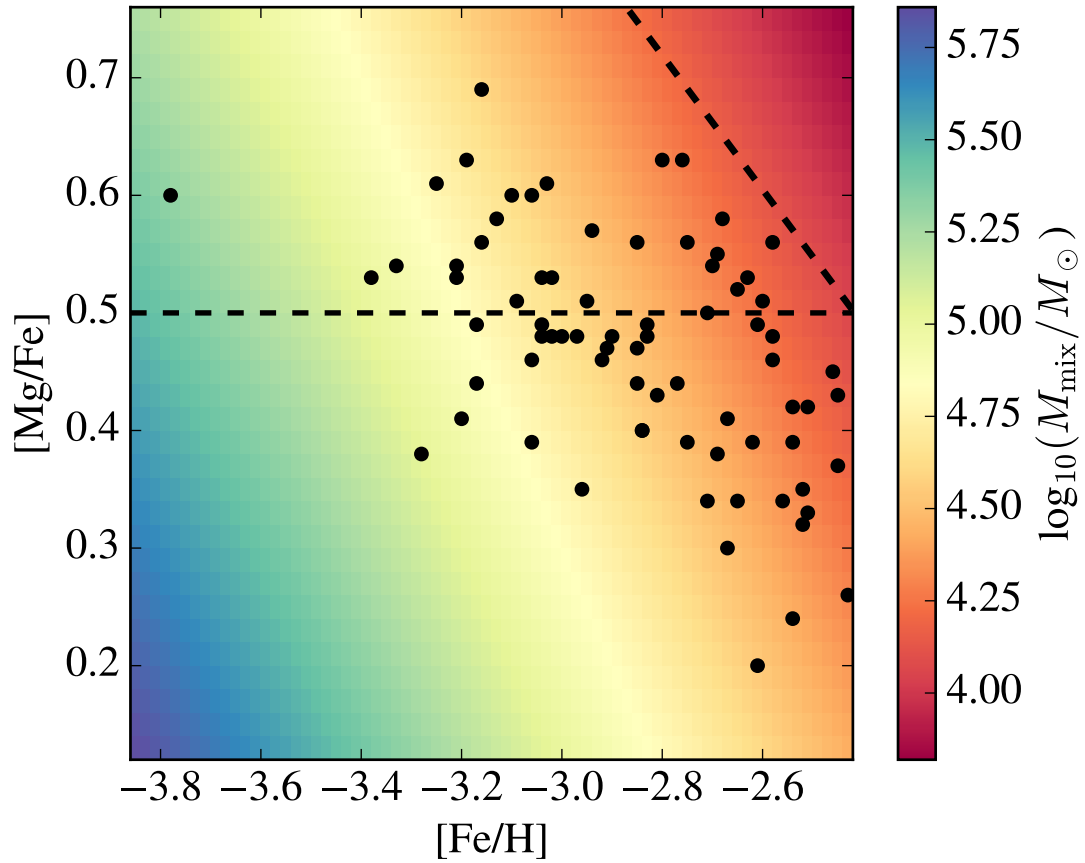
Figure 3.4: Same as Fig.1, but now showing in color the amount of mass with which our fiducial Mg mass of 0.1 $M_\odot$ would need to be mixed in order to explain the observed stellar abundances for our reduced sample. As metallicity increases and the ISM converges toward the yields, the amount of ISM over which ejecta is enriching decreases.

not only second and third. As seen in Figure 3.5, the demand that Eu (and hence the entirety of the r-process elements) traces the Mg results in total r-process masses well above 10^{-5} $M_\odot$. This serves as a proof by contradiction: requiring that the channel providing Mg enrichment in the early universe is the same as that which provides Eu would drastically overproduce the total r-process mass in the galaxy today.

We note that M_mix should be inversely proportional to the rate of injection, i.e. that rarer events will be spread out farther in distance as well as time, and will thus dilute further between events, e.g. through turbulent diffusion. In this way, this experiment implies another lower limit on M_rp. Any event that is rarer implies a mass per event higher than seen in Figure 3.5, and any event with higher rates would overproduce the galactic r-process even more drastically.

3.5 Discussion

By looking at metal-poor stars in the MW, we are able to place strong constraints on the mass per event and hence rate of the events that have enriched them in r-process elements. As seen in Figure 3.2, essentially all of the main r-process mass in the galaxy must have been synthesized in events that output $> 2.2 \times 10^{-6}$ $M_\odot$ of material, translating to a rate of $< 10^{-2}$ yr^{-1} in order to match $\dot{M}_\mathrm{r\text{-}p}$. This shows that even under the most conservative assumptions, core-collapse SNe are inconsistent with being the dominant progenitor of main r-process elements in the early universe given their frequency. On the other hand, our results for Sr show that this channel could still produce a sizable fraction of the light r-process elements.

Our conclusions regarding the main r-process are in agreement with several recent arguments , as it is only in the past few years that observations have

40
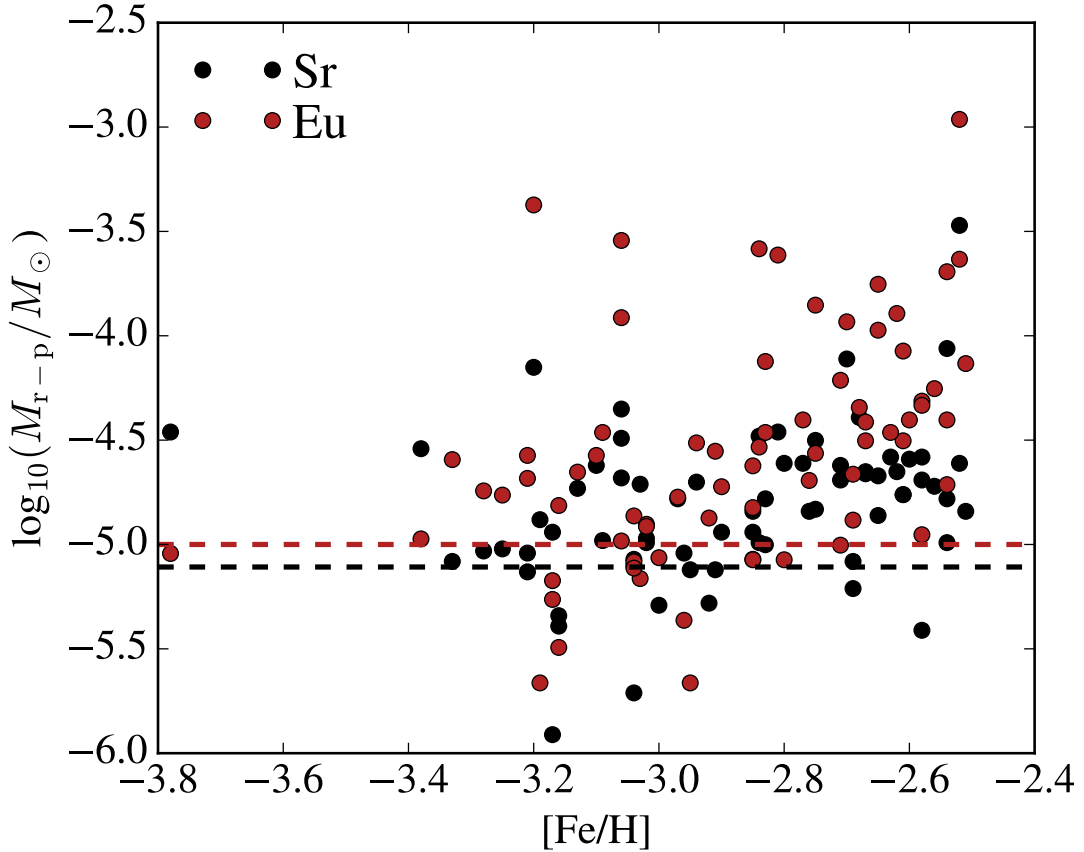
Figure 3.5: Total *r*-process mass per event required to explain the stellar abundances assuming it mixes over the same mass as the Mg as a function of metallicity. Eu is shown with red symbols, and black symbols show the inferred masses for Sr. The markers at the top left are not detections.

allowed us to break the degeneracy between rate and mass per event amongst the leading theories by looking farther back into the history of the galaxy (e.g., Shen et al., 2015; Ji et al., 2016a). In addition, we have used a fiducial density of 10^2 cm^{-3} in our calculation of M_{cool}, whereas NSMs are likely to occur in regions of lower density if they receive a kick from the SNe that created the pair (e.g., Belczynski et al., 2006; Kelley et al., 2010). From Equation (3.1), lowering the ambient density by a factor of 100 increases the mass per event by a factor of 4, implying an *r*-process mass of $\gtrsim 10^{-3}$ $M_\odot$ per event.

Beniamini et al. (2016b) have recently performed a similar analysis using ultra-faint dwarf galaxies (UFDs), assuming a gas mass for the galaxy and calculating the Eu (and hence total r-process) mass required to explain the observed stellar abundances. Their result is in agreement with ours, i.e. they find that the Eu mass per event is inconsistent with enrichment from typical core-collapse SNe given their rate, which naturally extends itself to MW stars assuming the dominant mechanism is the same in both galaxy types. This assumes that the ejecta are well mixed throughout the UFD gas, an assumption that we also require at the cooling mass scale, although this is well justified as SN remnants show efficient mixing well before the cooling mass is reached (Lopez et al., 2011). Even though inhomogeneous mixing may take place at larger scales, this will not re-concentrate a given element. However, our analysis demands an even more conservative lower limit on the r-process mass per event, as most of our cooling masses are below the fiducial 10^5 $M_\odot$ UFD gas mass.

Through independent means, we are able to look at both the first-peak and main r-process elements and calculate the total r-process mass implied by assuming that the source that provided them also generated 0.1 $M_\odot$ of Mg and scaling the r-process elements to solar abundances. We find that the implied mass per event for Eu production in most of our stars is $\gtrsim 10^{-5}$ $M_\odot$ and up to $\approx 10^{-3}$ $M_\odot$ of total r-process material. We also find that only a small fraction of first-peak r-process (Sr) production is consistent with a mass per event of $\lesssim 7.8 \times 10^{-6}$ $M_\odot$. However, this result is dependent on our assumption of 0.1 $M_\odot$ of Mg being ejected in the explosion. For example, a sizable fraction of the stars would become consistent with a mass per event of $\lesssim 7.8 \times 10^{-6}$ $M_\odot$ for a fiducial Mg mass of 0.03 $M_\odot$.

This implies that standard core-collapse SNe (i.e. those responsible for the

majority of Mg production) are not in perfect agreement with being the dominant source of first-peak r-process elements in the early universe, and by extension, that there may be multiple sources of r-process production, consistent with findings by Surman et al. (2014) and Ji et al. (2016d).

3.5.1 Distinguishing between Rare Events by Environment

This simple analysis lends itself to the mounting evidence that the source(s) of main r-process elements must be rare and yield high masses per event. Today, the two most promising candidates are NSMs (e.g., Lattimer & Schramm, 1974a; Rosswog et al., 1999a; Metzger et al., 2010a; Roberts et al., 2011a; Barnes & Kasen, 2013; Bauswein et al., 2013; Grossman et al., 2014; Ramirez-Ruiz et al., 2015) and jet-driven supernovae (e.g., Winteler et al., 2012; Nishimura et al., 2015), both of which occur at $\lesssim 1\%$ of the average CCSN rate and may inject relatively high masses into the ISM per event. Here we focus our efforts on attempting to distinguish between these two scenarios.

While several simulations of NSMs have found the explosion energy to be between 10^{50-51} erg, the maximum energy extractable from a neutron star that gives birth to a magnetar is not as well constrained. Metzger et al. (2015) have found that the birth of a magnetar may be accompanied by an injection of 10^{52-53} erg of energy if the rotational energy is extractable. Figure 3.6 shows how the constraints implied by our cooling mass argument change by varying the energy of the explosion. While we find that standard CCSNe are incompatible with any reasonable explosion energy, the energy implied by the spin-down of a magnetar in a jet-driven SNe places lower limits on the mass per event of $\gtrsim 10^{-2}\ M_\odot$. Although the data are not yet able to discern between NSM and rare SNe based on energetics, they demand a high mass per event and a rate much lower than
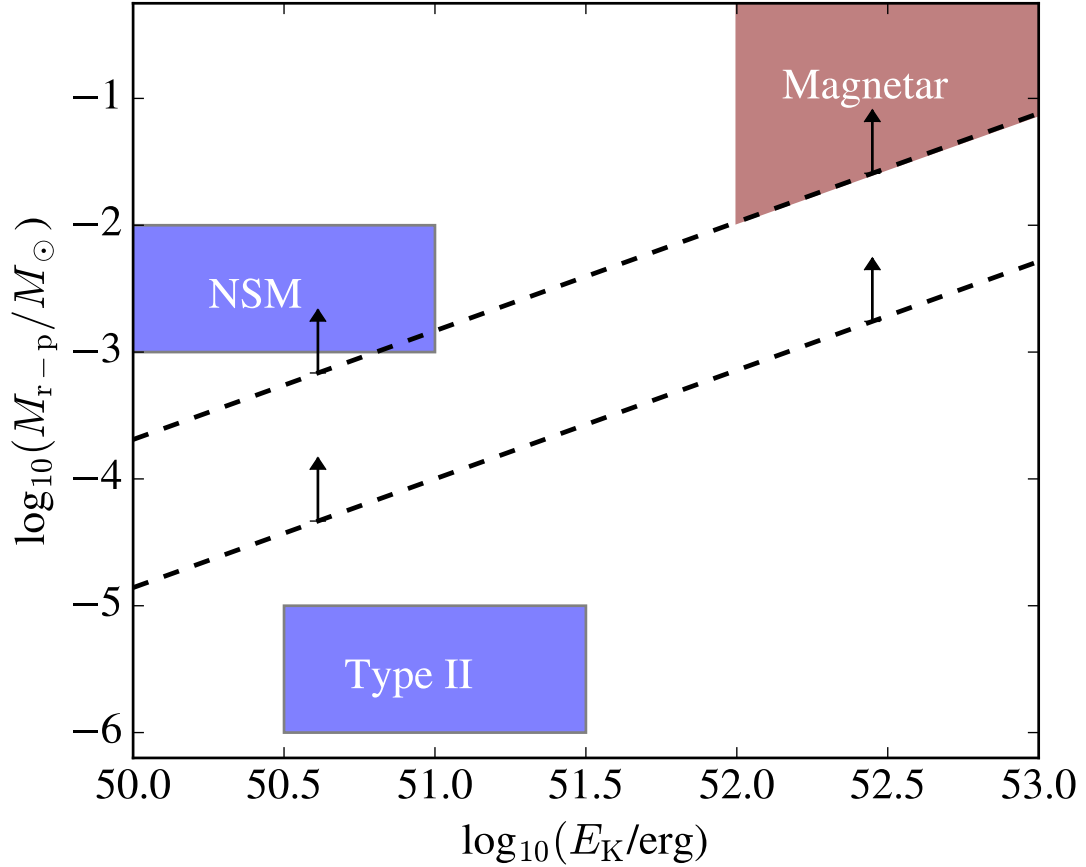
Figure 3.6: Inferred lower limit on r-process ejecta mass based on M_{cool} from Section 3.4. The dashed lines represent the 100 % and 50% values for the mass-weighted cumulative histogram as seen in Figure 3.2. This argument rules out Type II SNe (purple region denotes the range of current theoretical estimates) as the dominant contributor to the r-process mass budget at low metallicities, and puts constraints on the ejecta mass required in scenarios involving magnetars (maroon region).

that of typical type II SNe (based on our cooling mass argument), as well as a Mg mass much greater than 0.1 $M_\odot$ if the Mg is at all coupled to the Eu, as the masses inferred in Figure 3.5 would be too low to be consistent with a rare event (based on our mixing mass argument).

In addition to the somewhat weak energetic constraints between the two models, we may also consider the possibility that the two mechanisms may take place in different environments. NSMs must be preceded by two SNe, which are higly likely to impart linear momentum to the binary due to a combination of sudden and asymmetric mass loss (e.g., Behroozi et al., 2014). This may result in the binary merging within a shorter timescale (Beniamini et al., 2016a) and in a region far from its birthplace, enriching an environment that is chemically distinct. In contrast, the collapse of a massive star will occur on a timescale of ~ 10 Myr, not allowing the star to migrate far from its birthplace and possibly still within its birth cluster. In particular, if the jet-driven supernovae are some fraction f_{SN} of all standard CCSNe, then we expect the local environment to be enriched with the ejecta of $1/f_{\mathrm{SN}}$ SNe throughout the lifetime of the cluster, assuming a typical cluster dispersal time of a few Myr.

If the ejecta of the standard SNe and jet-driven SN are well mixed, the expected value for the ratio of r-process material to standard α-elements is given by the ratio of their respective production rates. Comparing this mass ratio to solar values, we obtain

$$[\mathrm{Eu/Mg}]_{\mathrm{jsn}} \approx -0.7 + \log_{10}\left[\frac{\dot{M}_{-7}^{\mathrm{r\text{-}p}}}{\dot{M}_{-3}^{\mathrm{Mg,ccsn}}}\right], \qquad (3.6)$$

where $\dot{M}_{-7}^{\mathrm{r\text{-}p}}$ and $\dot{M}_{-3}^{\mathrm{Mg,ccsn}}$ are the average r-process and Mg production rates in units of 10^{-7} and 10^{-3} $M_\odot \,\mathrm{yr}^{-1}$, respectively. Note that this is independent of f_{SN}, as varying the fraction varies both the Eu yield required per event as constrained
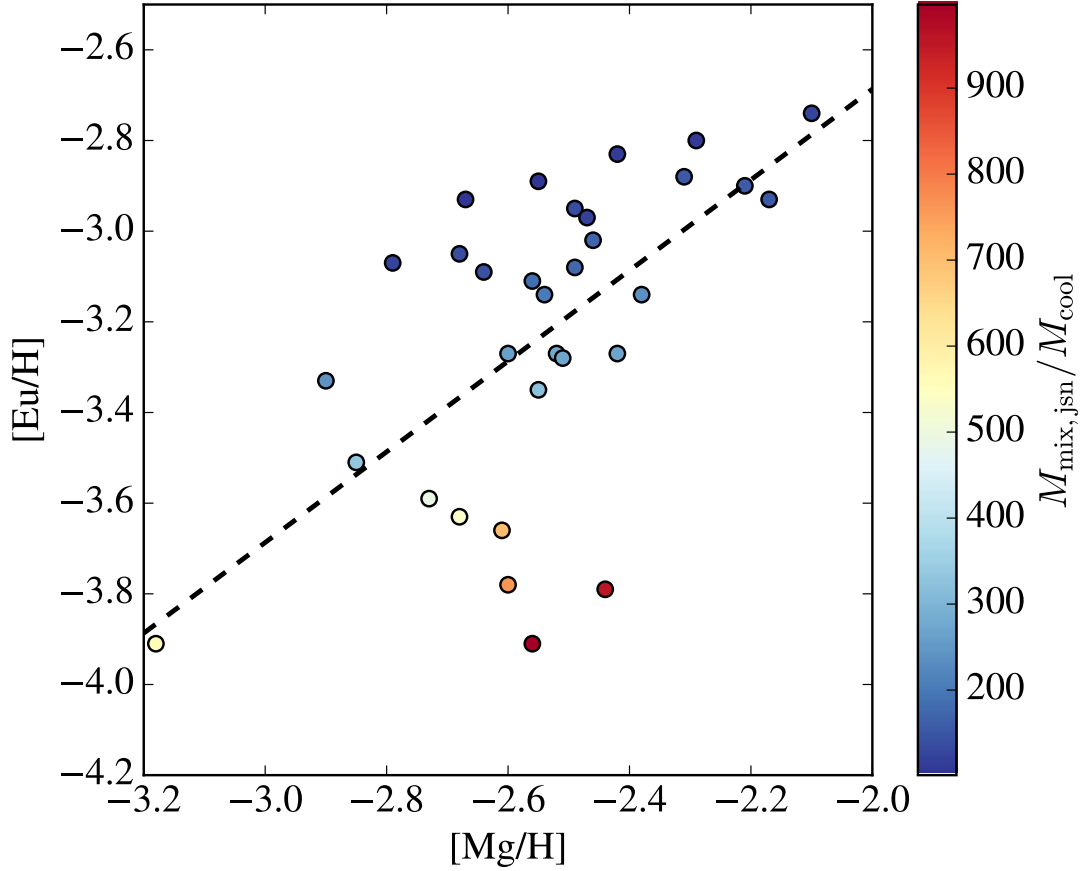
Figure 3.7: Eu and Mg abundances for our sample with the value for well mixed ejecta of one jet-driven SN and its corresponding $1/f_{SN}$ "normal" SNe shown with a dashed line. The colorbar shows the ratio of the mixing mass for Eu to the combined cooling mass of the other SNe, independent of f_{SN}.

by $\dot{M}_{\text{r-p}}$ and the number of accompanying SNe in the same way.

Figure 3.7 shows [Eu/H] and [Mg/H] for our sample, with the dashed line showing [Eu/Mg] expected for a well-mixed cloud of normal and jet-driven SNe. Here we restrict our sample to only include those where $M_{\text{mix}}/M_{\text{cool}} > 1/f_{SN}$ for a fiducial f_{SN} of 10^{-2} to isolate the stars whose ejecta would have likely mixed over all accompanying SNe. The sample of stars roughly falls along this line, but with significant scatter above and below. Whether this roughly order-of-magnitude scatter in [Eu/H] for a given [Mg/H] is indicative of chemical decoupling between

the production sites of Mg and Eu, or simply a result of inhomogeneous mixing is difficult to discern within this simple framework.

3.6 Conclusions

In this paper, we have used simple physical arguments to calculate lower limits on both first-peak and main r-process masses ejected within a single event. We have found, in congruence with other studies, that the implied masses are inconsistent with the rate of typical core-collapse supernovae, and instead are indicative of a rarer event.

Because only considered single-event candidates, this analysis does not allow us to comment on the trends with metallicity and/or time, which must rely on more detailed galactic chemical evolution (GCE) models. However, we are providing constraints on a critical parameter used in these models, specifically, we provide a minimum yield of Eu per injection event to be used in any GCE model. Our most r-process enhanced star in Figure 3.2, with a cooling mass of $1.3 \times 10^4\ M_\odot$, requires by Equation 3.2 an Eu yield of $M_{\mathrm{Eu}} > 10^{-6}\ M_\odot$. This is at least a factor of 30 larger than the Eu yield of $\sim 3.7 \times 10^{-8}\ M_\odot$ used in GCE models that consider CCSNe as the dominant source of Eu in the MW (e.g. Travaglio et al., 2004; Qian & Wasserburg, 2007).

By considering the environment in which these rare SNe may take place, we find that the abundances of the α-elements, particularly Mg, are marginally consistent with a fully mixed cloud of the rare SN and corresponding standard CCSNe ejecta, but with significant scatter. This assumes that the ejecta are all well mixed by the time the next generation of stars forms. The extent to which this assumption holds remains unclear, as inhomogeneous mixing of Population III SN ejecta may provide a plausible explanation for the carbon-enhanced metal-poor stars

(Sluder et al., 2016) as well as the chemical diversity observed in some UFDs (Ji et al., 2016c). In contrast, the uniformity of Mg abundances in low-metallicity halo stars points to efficient mixing occuring after the first SNe. Future observations of abundances in the lowest metallicity stars, in tandem with more detailed hydrodynamical simulations of mixing in the early universe, are needed to shed light on the nature of this discrepancy.

While uncertainties remain in distinguishing these rare events, the assumptions made regarding the cooling mass remain minimal and result in a conservative lower limit regarding the mass of r-process elements synthesized in individual production events. This analysis may lend itself to helping constrain the progenitor(s) of the so-called lighter element primary process (e.g. Travaglio et al., 2004; Montes et al., 2007) by studying abundances of the first- and second-peak r-process elements as well as their star-to-star variations, which will be the topic of future studies.

Chapter 4

Constraints on Collapsar

r-process Models through Stellar

Abundances

4.1   Chapter Abstract

We use observations of heavy elements in very metal-poor stars ([Fe/H] < -2.5) in order to place constraints on the viability of collapsar models as a significant source of the r-process . We combine bipolar explosion nucleosynthesis calculations with recent disk calculations to make predictions of the observational imprints these explosions would leave on very metal-poor stars. We find that a source of low ($\approx 0.1 - 0.5$ $M_\odot$) Fe mass which also yields a relatively high (> 0.08 $M_\odot$) r-process mass would, after subsequently mixing and forming new stars, result in [r/Fe] abundances up to three orders of magnitude higher than those seen in stars. In order to match inferred abundances, 10-10^3 $M_\odot$ of Fe would need be efficiently incorporated into the r-process ejecta. We show that Fe enhancement

and hence [r/Fe] dilution from other nearby supernovae is not able to explain the observations unless significant inflow of pristine gas occurs before the ejecta are able to form new stars. Finally, we show that the inferred [Eu/Fe] abundances require levels of gas mixing which are in conflict with other properties of r-process enhanced metal-poor stars. Our results suggest that early r-process production is likely to be spatially uncorrelated with Fe production, a condition which can be satisfied by neutron star mergers due to their large kick velocities and purely r-process yields.

4.2   Introduction

The gravitational wave discovery of the binary neutron star merger (NSM) GW170817 (Abbott et al., 2017b) along with the intensive multi-wavelength electromagnetic observations of the ensuing kilonova SSS17a/AT2017gfo (e.g., Coulter et al., 2017b; Cowperthwaite et al., 2017; Drout et al., 2017b; Shappee et al., 2017) provided definitive evidence of NSMs being a viable source of r-process elements in the galaxy and universe as a whole. Since then, a number of interesting questions have arisen regarding the physics of NSMs as well as the implications of NSMs being the only significant source of the r-process throughout cosmic time (see Siegel, 2019, for a summary of current issues with the merger-only model).

One puzzle exhibited by the kilonova is the large mass of lanthanide rich ejecta (≈ 0.035 $M_\odot$) inferred through modeling (e.g., Kasen et al., 2017a). While the mass of dynamical ejecta expelled by tidal forces is expected to be at most $\approx 10^{-2}$ $M_\odot$ (e.g., Radice et al., 2018a), the kilonova required several times this mass in order to explain the peak luminosity and subsequent evolution. This requires an additional source of heavy r-process ejecta, with one theoretically predicted candidate being outflows from a remnant accretion disk. These outflows, which

originally were thought to be powered by neutrino irradiation and thus result in a relatively weak r-process , may be instead launched by nuclear recombination and viscous dissipation, maintaining a low Y_e and resulting in a heavy r-process (e.g., Wu et al., 2016a).

In addition, while numerous studies have implicated a rare (in comparison to standard core-collapse supernovae) channel for the r-process at both early and late times (Hotokezaka et al., 2015; Ji et al., 2016b; Macias & Ramirez-Ruiz, 2018), some issues have arisen with NSMs being a dominant channel in the context of galactic chemical evolution. In particular, the expected / observed delay time distribution t^{-1} of NSMs predicts a flat [Eu/Fe] trend in stars with [Fe/H] metallicities > -1, where we use the standard notation [El/H] = $\log_{10}(N_{El}/N_H) - \log_{10}(N_{El}/N_H)_\odot$, where N_{El} is the column density of a given element. This is not seen in the data, as the [Eu/Fe] exhibits a "knee" at around [Fe/H]=-1, similar to that of alpha elements produced in CCSNe. This discrepancy implies that there may be another early, possibly dominant, channel of r-process production that has yet to be directly detected (Côté et al., 2018), or that the delay-time distribution of NSMs differs from that of Type Ia supernovae (e.g., Simonetti et al., 2019).

One solution recently detailed by Siegel et al. (2019) is the collapsar model proposed by Woosley (1993), in which the core of a massive ($\gtrsim 30\ M_\odot$) rotating star collapses to form a black hole. The resultant explosion does not unbind the entirety of the star, leaving behind material with sufficient angular momentum to form an accretion disk (MacFadyen & Woosley, 1999; Lee & Ramirez-Ruiz, 2006). Due to the large ($> 10^{-3} M_\odot\ \mathrm{s}^{-1}$) accretion rates achieved at early times, the midplane of the disk may attain high enough density to suppress positron creation, thus capturing electrons only and producing neutron rich material. The

ejection of this material through a disk wind would then produce a strong r-process . This scenario, motivated by the inferred accretion disk winds of SSS17a, would result in significant heavy element production immediately following star formation events, thus reproducing the trend in [Eu/Fe] at late times. However, due to the large progenitor masses required, collapsars are inherently rare (even compared to NSMs) and must produce a large mass of r-process ejecta per event in order to be consistent with the average mass production-rate inferred for the Milky Way of $\sim 10^{-7}$ $M_\odot$ yr^{-1} (Bauswein et al., 2014).

Here we discuss the implications of such large r-process ejecta masses and compare to observations of stars that have been formed from gas that has been enriched by at most a few nucleosynthetic production events. In Section 4.3, we derive predictions for stellar abundance measurements within the collapsar scenario to compare to observations of very metal-poor stars and discuss mixing of the r-process elements. In Section 4.4 we comment on the implications of our findings in the context of r-process progenitors.

4.3 An Observational Constraint on the Collapsar Model

4.3.1 Comparison with Theoretical Models

In order to make predictions of [r/Fe] for our sample stars, we employ the nucleosynthesis calculations of Maeda & Nomoto (2003). They calculate bipolar (jetted) explosion models of 25 and 40 $M_\odot$ stars while varying energy and opening angle as well as spherical "normal" supernovae. We include results for only their bipolar explosions though the spherical results are qualitatively indistinguishable. We do not include their model 40D, which would have the largest discrepancy
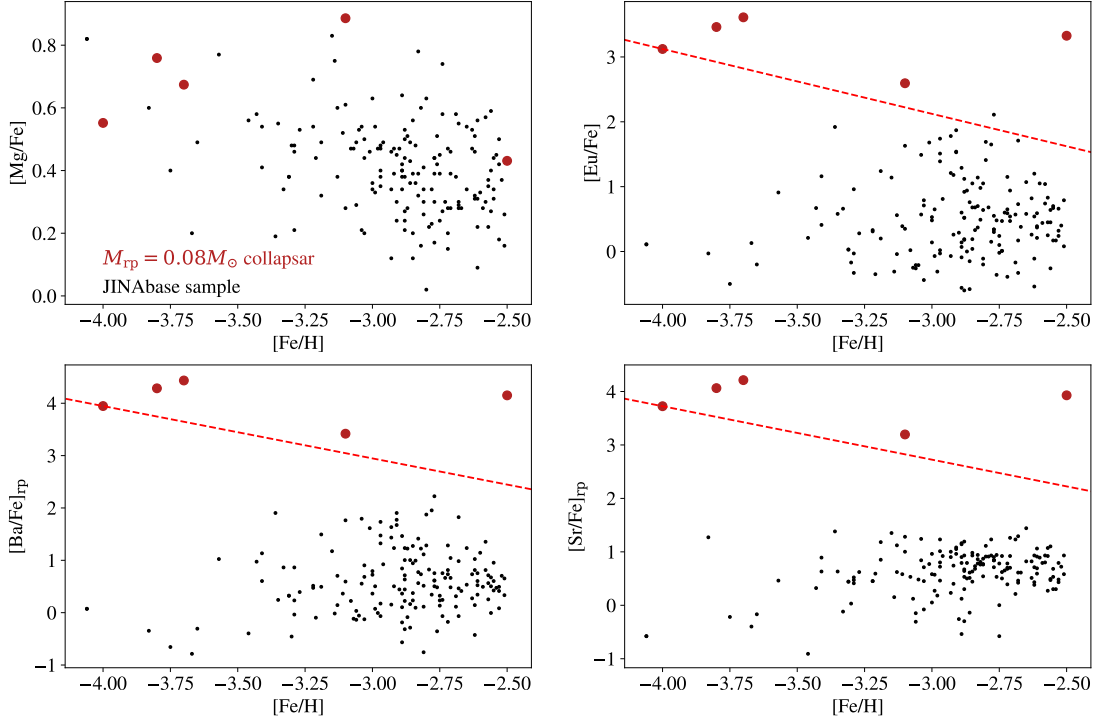
Figure 4.1: Stellar abundances from JINAbase are shown in black along with single-event predictions from the collapsar models of Maeda & Nomoto (2003) combined with r-process calculations from Siegel et al. (2019) in red. Average error bars are ~ 0.2 dex for the data. While the alpha element Mg is in agreement with the data, the r-process abundances are much higher than seen in observations. Shown in the dashed line is the trajectory a parcel of gas would take due to dilution in Fe from nearby supernovae that provide Fe but no r-process elements.

with the observational data due to an anomalously low Fe mass of $\sim 10^{-7}\ M_\odot$ caused by a larger initial remnant mass.

These calculations provide us with Fe and Mg yields, as well as the [Fe/H] which depends on the mass over which the explosion diluted, given by

$$M_{\mathrm{dilution}} = 5.1 \times 10^4 M_\odot E_{51}^{0.97} n_1^{-0.062} C_{10}^{-9/7}, \tag{4.1}$$

where E_{51} is the explosion energy in units of 10^{51} ergs, n_1 is the ambient hydrogen number density in units of 1 cm^{-3}, and C_{10} is the local sound speed in units of 10 km s^{-1} (Shigeyama & Tsujimoto, 1998). The Fe masses they obtain range between 0.078-0.54 $M_\odot$. The calculations do not follow the nucleosynthesis in a remnant accretion disk and focus on the explosion itself, as the full calculation remains computationally prohibitive. Instead, we combine their calculations with the recent work by Siegel et al. (2019), in which only the remnant accretion disk is simulated and r-process nucleosynthetic calculations are performed.

In order to derive a mass of r-process elements necessarily synthesized in a single collapsar event to explain the Milky Way production rate, Siegel et al. (2019) convolve the long GRB and star formation rate with the average mass production of r-process elements in the Milky Way in order to derive a mass of $0.08 - 0.3\ M_\odot$ per event given the uncertainties. This is attainable within their simulations, thus introducing the viability of the collapsar model within their framework. In our analysis we adopt their lowest event yield of 0.08 $M_\odot$, thus deriving a lower bound on the expected [r/Fe] abundances.

After the collapsar event, the r-process material formed within the disk should efficiently mix with the ejecta synthesized in the explosion, thus leaving behind a chemical imprint on the subsequent generation of stars formed. With this, we are able to derive a simple equation to determine the expected [r/Fe] enhancement

given by

$$[r/\text{Fe}] = \log_{10}(M_\text{r-p}/M_\text{Fe})_\text{collapsar} - \log_{10}(M_\text{r-p}/M_\text{Fe})_\odot, \qquad (4.2)$$

where $M_\text{r-p}$ and M_Fe are the total mass of r-process elements and Fe produced in either the collapsar or contained within the solar abundance pattern. The solar abundance pattern is taken from Lodders (2003) and the r-process residual pattern from Arnould et al. (2007). For the solar r-process pattern, we consider elements starting from mass number A=69.

This can be directly applied to any r-process element, assuming a solar abundance pattern is attained within the total r-process mass. The application of this equation to the lighter r-process elements may be less justified, as there is evidence of some variation within e.g. first-peak elements compared to the Sun. However its application to heavier elements is observationally motivated by the robustness of the heavy r-process solar pattern across decades in [Fe/H] metallicity (e.g., Frebel, 2018).

To test this prediction, we utilize JINAbase (Abohalima & Frebel, 2018) to gather stars with an [Fe/H] metallicity of $<$ -2.5, from which measurements have also been made of Mg (alpha), Sr (first peak), Ba (second peak), and Eu (lanthanide). We employ an additional cut of [Ba/Eu] $<$ -0.5 in order to avoid any early s-process contaminants (Simmerer et al., 2004). We do not include stars with upper-limits on any of the elements we are considering. This brings our total sample to a size of 186 stars. At these low metallicities, stars formed should retain memory of at most a few nucleosynthetic events having polluted the gas from which they form (Audouze & Silk, 1995; Shigeyama & Tsujimoto, 1998).

With this we are able to directly compare the observations of heavy element abundances in our sample with predictions of the collapsar scenario. The results

for Eu, Ba, and Sr are shown in Figure 4.1. We compare against the solar r-process values for Sr and Ba by adjusting for the fact that the s-process contribution to the present day solar pattern is 75% and 85%, respectively. This only results in an offset in our plot as the correction is applied to both data and the models and does not inform any differences between them. As can be seen, the collapsar models consistently over-predict the observations of heavy elements. The top left panel shows the good agreement between predictions for Mg and our sample that is not seen in the r-process elements. We note that the largest discrepancies of $\sim$ 3 dex exist at the lowest metallicities, where the single-event assumption is most justified.

We assume that at large scales the ejecta mix efficiently, motivated by hydrodynamic simulations of the expansion of both collapsar jets and NSM tidal ejecta losing anisotropy early in their evolution (Ramirez-Ruiz & MacFadyen, 2010; Montes et al., 2016). However, any geometric effects (e.g. disk winds being more focused along the midplane) would only serve to concentrate the r-process material, thus increasing the predicted $[r/\text{Fe}]$ and exacerbating the discrepancy. Furthermore, though the Y_e electron fraction distribution may have a significant effect on limited to main r-process abundance ratios compared to Solar, the fact that the model predictions overshoot the data near all three r-process peaks does not allow for any reasonable abundance distribution to relieve the tension. For example, moving all of the r-process ejecta closer to the first peak, while conserving total mass, would only increase the predicted $[\text{Sr}/\text{Fe}]$.

One possible resolution would be the dilution of $[r/\text{Fe}]$ by typical core collapse supernovae that may not provide significant r-process enrichment. The red dashed line shows the result of such dilution. Since the Fe enhancement would only increase the denominator on the y-axis while increasing the numerator on

the x-axis, this would result in the plotted line with slope -1 through the plot. This line does not intersect the data more than marginally for any star and is thus still difficult to reconcile with the observations. It may be possible however that the [r/Fe] of the gas is enhanced with Fe from many nearby supernovae, taking it downward along the red trajectory drawn in Figure 4.1. Then, at [Fe/H] metallicity of ∼-2 is diluted in both Fe and Eu equally by pristine inflowing material, lowering the [Fe/H] and pushing it horizontally back toward the data.

Another possibility is continued expansion of an Eu and Fe-containing collapsar ejecta mixing significantly beyond M_{dilution}. If material expands into ejecta from many nearby supernovae, it will not maintain the [Eu/Fe] characteristic of its own yields, but rather obtain an [Fe/H] (and thus [Eu/Fe]) corresponding to the average [Fe/H] of the combined sources. Although this would violate the long-held and often utilized "single-event" nature of these stars, which has been used to compare to lighter element abundances against SN models, we discuss the implications of this scenario below.

4.3.2   Observational Implications within the Collapsar Model

As mentioned above we can also ask the inverse question from our JIN-Abase sample. That is, given the inferred [Eu/Fe] and assuming an Eu mass of $M_{\mathrm{Eu,collapsar}} = X_{\mathrm{r\text{-}p},\odot}^{\mathrm{Eu}} M_{\mathrm{r\text{-}p,collapsar}} = 8 \times 10^{-5} M_{\odot}$, we can invert Equation 4.2 to solve for the mass of Fe that the Eu mixes with. Furthermore, we can then calculate the mass of pristine material that the total Fe must be spread over in order to maintain the low [Fe/H]. This method is independent of the models of Maeda & Nomoto (2003), as we now take the [Eu/Fe] abundances from our sample as an input to the equation as opposed to just comparing against them.
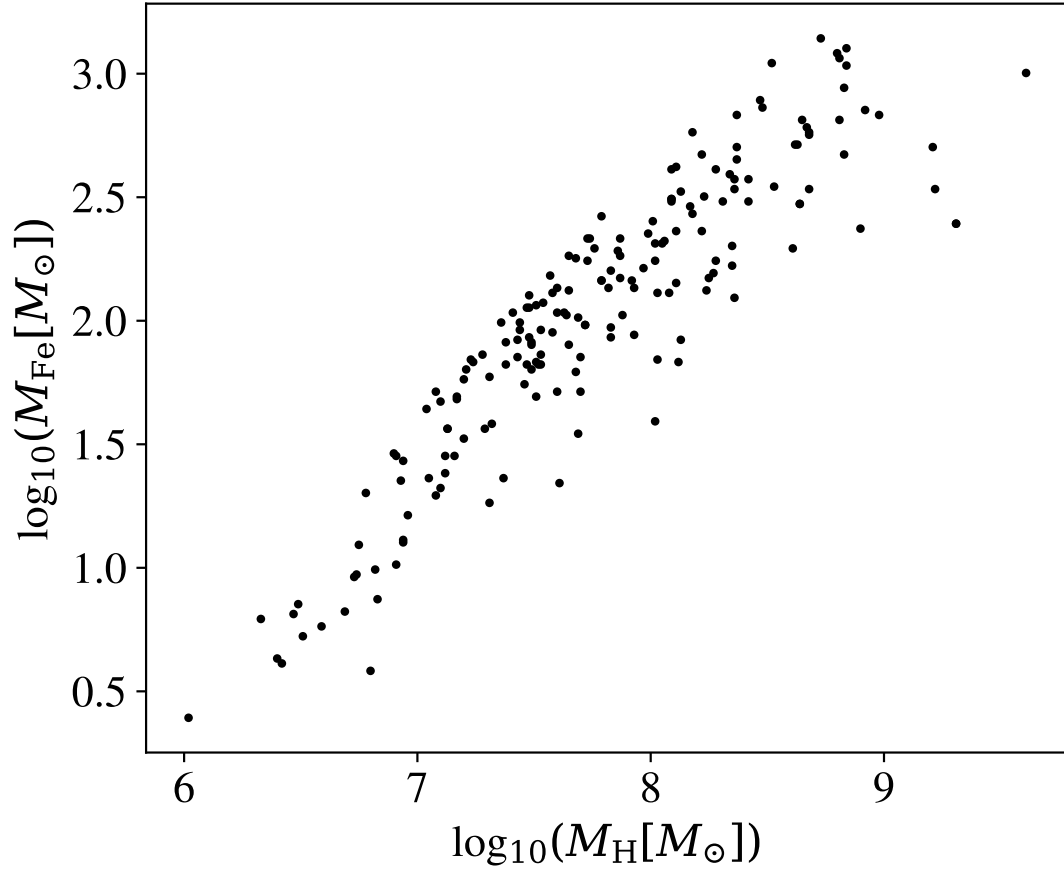
Figure 4.2: Fe mass mixed with Eu producing events required to explain inferred [Eu/Fe] abundances are shown along the y-axis, and total Hydrogen mass in order to maintain the [Fe/H] in the stars is shown on the x-axis for our JINAbase sample of stars.

Figure 4.2 shows the result of this experiment. We immediately see a $\sim 10^3$ dynamic range in both the inferred swept Fe masses and the Hydrogen dilution masses necessary to reproduce the observations. In the most extreme cases, we find Hydrogen dilution masses of $\approx 10^9$ $M_\odot$. This is well beyond the typical dilution masses of $\sim 10^4$ $M_\odot$, requiring a very large-scale mixing process which may be disfavored by the observed dispersion of r-process element abundances at early times, the rarity of the r-I/II stars ([Eu/Fe] $> +0.3$), as well as disputing the single-event nature of stars below our [Fe/H] < -2.5 selection.

We propose that a more likely resolution is that the r-process production site is spatially uncorrelated with any Fe production, and thus the r-process material is naturally diluted by the time it comes into contact with any Fe (Shen et al., 2015; van de Voort et al., 2015; Naiman et al., 2018). This may be the case for a NSM, in which substantial kicks during the preceding SNe may push NSM progenitors far from their birthplace before merging. While this argument does not solve the outstanding puzzle of the [Eu/Fe] "knee" seen in the chemical evolution trend, it does argue against an r-process source synthesizing Fe, unless its mixing process is extreme.

4.4   Discussion

Our analysis finds that any r-process source that is physically associated with Fe production seems to be disfavored by observations of heavy elements within very metal-poor stars. While this finding is consistent with aspects of previous analyses (c.f., Qian & Wasserburg, 2007, and references therein), we place direct constraints on the collapsar model of r-process enrichment. This poses a challenge to the collapsar scenario, instead lending further credence to a NSM or NS black-hole (NSBH) merger that should result in minimal Fe production and likely take

59

place far from their birth sites.

This does not rule out standard CCSNe as a source of a lighter r-process , as they may produce substantially less e.g. Sr per event given their rates and may still be consistent with the abundances. The abundances also are not in conflict with a magnetorotational jet-driven supernova (Winteler et al., 2012; Nishimura et al., 2015), as the mass of r-process is decreased by a factor of 10 and still consistent with most of the data in Figure 4.1 provided external Fe enhancement. However, this scenario may require very high ($\sim 10^{13}$ G) pre-collapse magnetic fields to produce elements such as Eu (Mösta et al., 2018).

Recent kinematic studies of the highly r-process enhanced r-II stars show evidence of clustering in phase space (Roederer et al., 2018), suggesting they may have been stripped from small dwarf galaxies like the highly r-process enhanced Reticulum II (Ji et al., 2016b). If this is the case, measurements of total r-process masses of say Eu may not be reliable, as the abundances may be driven by environmental effects such as low star formation efficiency in these galaxies as opposed to probing the event itself. However given their low gas mass, the amount of dilution shown in Figure 4.2 necessary to maintain both the [Eu/Fe] and [Fe/H] may be more difficult to attain. We also note that observations of r-process enhanced stars are biased toward the halo and thus may be probing a primarily ex-situ population. Future observations of r-process enhanced bulge MW stars may distinguish if the production scenario is different between these two components.

Crucial to our analysis is the assumption that the r-process elements are well mixed with the Fe by the time the next generation of stars form. As the Fe is primarily produced in a jet and the r-process may be launched in a more equatorially concentrated disk outflow, it is possible that their different ejection speeds

and times may inhibit efficient mixing, though again this may be in conflict with hydrodynamical simulations (Ramirez-Ruiz & MacFadyen, 2010; Montes et al., 2016). As an example, Martin et al. (2015) propose inefficient mixing between a polar and equatorial outflow as a possibility to explain the abundances seen in HD 122563, though they suppress the mixing between components by a factor of 50 as opposed to the $> 10^3$ suppression required for our lowest metallicity stars.

If this inefficient mixing scenario is what occurs, we are still able to state that the abundances in metal-poor stars observed argue against spatial correlation of r-process production with Fe, as this would result in a similar trajectory to those shown by the red dashed-lines in Figure 4.1. This spatial correlation is to be expected in a collapsar that explodes promptly following a star-formation event and would not have time to migrate far from its birthplace.

While SSS17a/AT2017gfo served as the long sought after direct evidence of significant r-process production in NSMs, there remain many outstanding questions regarding their role throughout cosmic time. There is certainly still room if not evidence for multiple progenitor channels contributing significantly. Future observations of electromagnetic counterparts to gravitational wave sources will continue to elucidate remaining open questions in r-process nucleosynthesis and hopefully reveal new mysteries to explore.

Chapter 5

Predicting Ensemble Kilonova Properties from Stellar Abundances

5.1 Chapter Abstract

The binary neutron star merger GW170817 has enabled observations of one of the most sought after events in transient astrophysics: the radioactive decay of freshly synthesized r-process elements, here referred to as the kilonova (KN) SSS17a/AT2017gfo. Intensive multi-wavelength observations of this object have yielded a treasure trove of information, including the presence of a strong blue component in the light curve at early times. While this feature alone provides critical constraints on KN models, it may take years before we can begin to say whether the properties (e.g. color evolution, ejecta masses) of SSS17a are common, or one realization of an intrinsically diverse set of outcomes as is expected from some simulations. In addition, the role of neutron star mergers and their resultant

KNe as a significant r-process at early times remains an open question. Here we attempt to answer these questions by looking at low-metallicity stars which are thought to have been enriched by at most a few r-process events. By using inferred abundances of Sr, an element created in a limited ($69 < A < 120$) r-process , and Eu which is synthesized in the main ($120 < A < 240$) r-process , we use a simple model to make postdictions of the KN that resulted from their creation. We find that observations of these elements allow for a broad range of KN properties and suggest observational strategies to accommodate this range. We also find that the ratio of red to blue ejecta masses inferred for SSS17a/AT2017gfo lies at the peak of our distribution, suggesting its properties may be relatively common amongst possible KN types. Future observations of KNe will be able to constrain them as a significant source of r-process in the early universe.

5.2 Introduction

GW170817 (Abbott et al., 2017c), in tandem with SSS17a/AT2017gfo (Coulter et al., 2017a; Drout et al., 2017a) and GRB 170817A (Abbott et al., 2017d,a), has ushered astronomy into the long awaited multi-messenger era and provided unprecedented insight into neutron star mergers (NSMs) and all of the physics they entail. In particular, the electromagnetic (EM) transient observed just 11 hours after the initial gravitational wave (GW) trigger served as the smoking gun in placing NSMs as a prominent astrophysical site for the production of the heaviest elements (Kasen et al., 2017b).

While theory has long held predictions for the outcome of the merger (Lattimer & Schramm, 1974b; Eichler et al., 1989; Li & Paczyński, 1998; Freiburghaus et al., 1999; Rosswog et al., 1999b; Metzger et al., 2010b; Roberts et al., 2011b; Goriely et al., 2011), both hydrodynamically as well as in coupled nucleosynthesis

calculations, a consensus has not yet been reached as to what the full element range produced would be, which has profound implications on the resultant color evolution of the emerging KN (Kasen et al., 2017b). Specifically, uncertainties in nuclear mass models, NS equation of state, lifetime of a hyper massive NS, and microphysics occurring in a remnant accretion disk have led to a large variation in the predicted electron fractions Y_e (and hence nucleosynthetic outcomes) that are realized in the ejecta (Wu et al., 2016b). Moreover, naturally varying binary parameters such as the binary mass ratio $q = M_2/M_1$ result in different disk masses (Radice et al., 2018b), hence different amounts of neutrino irradiation which allows for intrinsic variation even with all other physical ingredients held fixed. This has led to uncertainties as to whether only a main heavy r-process takes place in the (tidal) dynamical ejecta, or a relatively lanthanide poor, "limited" r-process accompanies the dynamical ejecta in the form of a disk-wind or dynamically squeezed polar ejecta (e.g., Kasen et al., 2017b)

Fortunately AT2017gfo has already shed light on this issue, as the early time light curve ($t \lesssim 1$ day) necessitates a strong blue component possibly composed of lanthanide free ejecta, in addition to a more slowly evolving, high opacity component coming from the dynamical ejecta (Kilpatrick et al., 2017; Coulter et al., 2017a; Drout et al., 2017a). This has provided the key insight not only that a limited r-process does take place in NSMs, but best fit KN models have provided the masses synthesized in each component (Villar et al., 2017; Kilpatrick et al., 2017; Kasen et al., 2017b). Models of SSS17a/AT2017gfo invoke masses of limited r-process material $M_{\mathrm{blue}} \approx 0.014\ M_\odot$ and main r-process material $M_{\mathrm{red}} \approx 0.034\ M_\odot$ (Kilpatrick et al., 2017).

While the detection and accurate model predictions of SSS17a/AT2017gfo are a triumph for both observation and theory, with only one KN observed in such

exquisite detail it remains difficult to infer anything about whether its properties are common amongst all KNe, though several studies have already begun hinting toward diversity (Gompertz et al., 2018; Ascenzi et al., 2019). Unfortunately, a KN sample large enough to provide statistically robust conclusions on this intrinsic variation may take many years to accomplish due to LIGO taking time to reach design sensitivity in addition to remaining uncertainties in the merger rate.

In this *Letter* we present a method to circumvent this bottleneck by looking at abundances in very metal-poor (EMP, [Fe/H]<-2.5) stars within the MW. In Section 5.3 we introduce the observations of these stars and discuss how they might serve as a fossil record of ancient KNe. In Section 5.4 we present our KN model and the resultant diversity in observational properties inferred from the stellar abundances and compare our results to SSS17a/AT2017gfo. In Section 5.5 we discuss our findings and suggest some possible observational strategies for future KN follow up.

5.3   Stellar forensics

The successful push toward increasing the number of observations of stars at the lowest [Fe/H] metallicities has led to the emergence of the field of galactic archaeology, in which abundances of stars within and around our own MW are used to infer clues about its early evolution. Recently, several studies have focussed on distinguishing between core-collapse supernovae and NSMs as the dominant site of r-process element production, with results pointing toward a relatively rare and high yield production event (Macias & Ramirez-Ruiz, 2018; Ji et al., 2016b; Beniamini et al., 2016b). These studies rely on low-metallicity stars with [Fe/H]$\lesssim -2.5$, which serve as fossil indicators of the (at most) few nucleosynthetic production events which enriched the gas from which they have formed (Audouze

& Silk, 1995; Shigeyama & Tsujimoto, 1998).

For our study, we focus on very metal poor stars which have detections of both Sr, an element which exists near the first peak of the solar r-process , as well as Eu and Ba, which exist beyond the first peak and are representative of a heavier r-process pattern. Although the Solar Sr and Ba abundances are produced in majority by the s-process, we employ a cut of [Ba/Eu] < -0.5 in order to avoid possible s-process contaminants (Simmerer et al., 2004). To isolate only stars which meet these specific criteria, we utilize JINAbase (Abohalima & Frebel, 2018), an online database which compiles observations of stellar abundances from the literature, ensuring consistency in e.g. solar abundance comparisons. Our sample of EMP stars with detections of both Sr as well as Eu totals 208.

Observations of r-process elements in low metallicity stars have shown extremely robust abundance patterns within the second and third (main) r-process peaks across orders of magnitude in [Fe/H] metallicity, while the first-peak elements have shown large variability (Sneden et al., 2008). Motivated by these findings, our analysis employs the following assumptions:

1. Sr is representative of all elements created in the limited r-process ($A \lesssim 120$), resulting in a lanthanide poor environment such as the hydronamically squeezed polar ejecta, and Eu production will serve as an independent emissary for the main r-process component synthesized in tidal tails and disk winds.

2. These two elements when observed in EMP stars, were created in the same event, one NSM in which the two components mixed together efficiently before the next episode of star formation.

Under these assumptions we can then infer that the observed mass ratio of
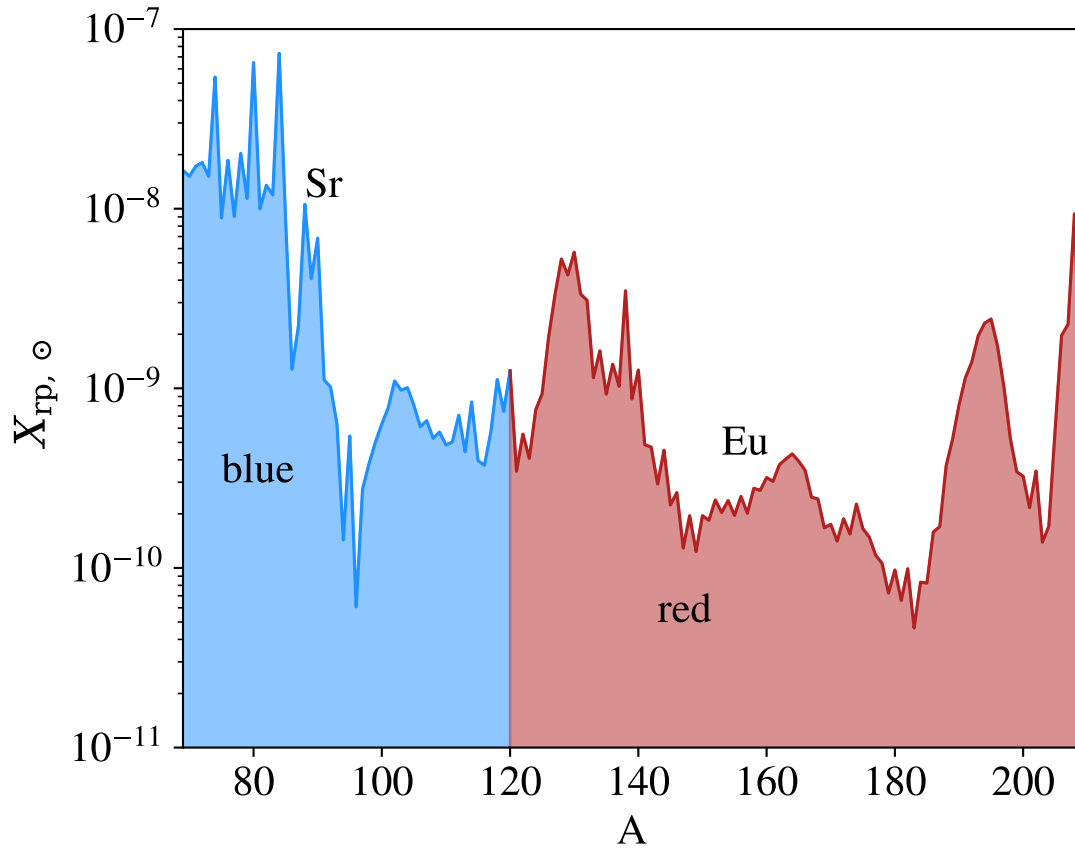
Figure 5.1: Solar r-process pattern taken from Arnould et al. (2007), along with colors indicating our cutoff between limited and main r-process (see text for discussion of the placement of the cutoff). Eu and Sr are labeled at their respective mass numbers A.

these elements in EMP stars is equivalent to the mass ratio of main to limited r-process products within the NSM ejecta, i.e.

$$\left[\frac{\text{Eu}}{\text{Sr}}\right] = \left[\frac{M_{\text{red}}}{M_{\text{blue}}}\right], \tag{5.1}$$

independent of the external mass over which the ejecta are diluted since the yield will be conserved assuming the ejecta are well mixed.

Figure 5.1 shows the solar r-process pattern and our distinction between elements associated with a red versus a blue component. We note that although the limited r-process pattern extends beyond our mass number cut, the actual mass produced is dwarfed by that produced in the main, by several orders of magnitude near the second peak. Thus an element near A of 120 will be primarily produced in a lanthanide rich environment corresponding to a red component.

Figure 5.2 shows our inferred red to blue mass ratios for our sample of EMP stars. The mass ratios follow a log-normal distribution with a mean of about 3 and a standard deviation of roughly a factor of three. SSS17a/AT2017gfo lies near the peak of our distribution, possibly indicating that it can be considered a relatively typical kilonova. This order of magnitude range in red to blue mass ratios translates directly into a diverse set of KN properties, as we explore in the following Section.

5.4 Kilonova reconstruction and relation to SSS17a/AT2017gfo

The red to blue mass ratios inferred in the Section 5.3 can be used to reconstruct the expected diversity of KN light curves provided that the mass of one of the components is known or can be estimated. To calculate the KN luminos-
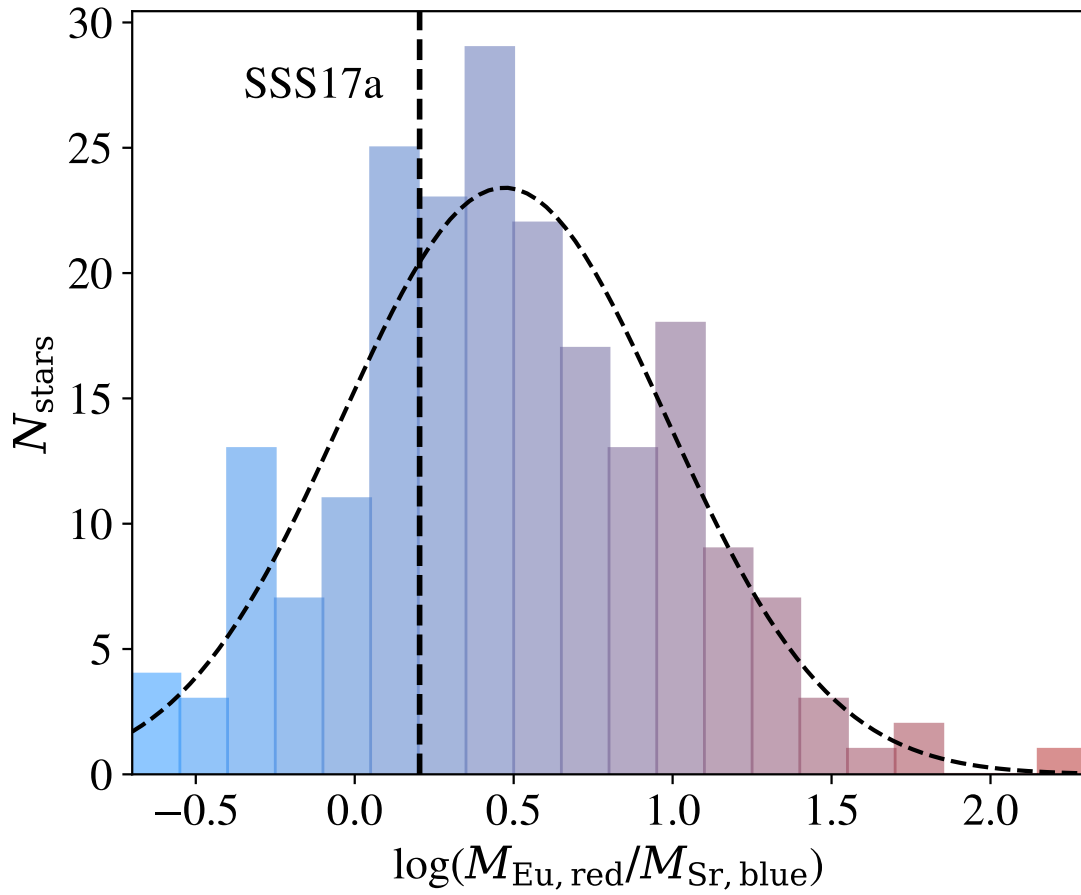
Figure 5.2: Inferred mass ratios of red to blue components as calculated from Equation 5.1 for our sample of EMP stars. Colors indicate the presence of lanthanide free to rich ejecta, from left to right.

ity we use a one-zone model following Metzger (2017) and Villar et al. (2017). This model considers an ejecta mass m_{ejecta} with an average velocity v_{ejecta}. The ejecta are composed of r-process elements and expand with a constant velocity distribution. In what follows, m is the mass coordinate with velocity $v(m)$.

The ejecta will heat and radiate energy due to r-process elements decaying with a heating rate

$$\dot{Q}(m) = mX_r(m)\dot{e}_r, \tag{5.2}$$

where $X_r(m)$ is the mass fraction of r-process elements, and the specific energy injection rate is estimated using a fitting formula from Korobkin et al. (2012),

$$\dot{e}_r = 4 \times 10^{18}\epsilon_{\text{th}}\left(0.5 - \frac{1}{\pi}\arctan[(t - t_0)/\sigma]\right)^{1.3}\frac{\text{erg}}{\text{s g}} \tag{5.3}$$

with $t_0 = 1.3$ s and $\sigma = 0.11$ s. The thermalization efficiency is taken to be the combination of various processes and fitted to be (Barnes et al., 2016):

$$\epsilon_{\text{th}} = 0.36\left[\exp\left(-a\left(\frac{t}{1\text{ day}}\right)\right) + \frac{\ln(1 + 2b(\frac{t}{1\text{ day}})^d)}{2b(\frac{t}{1\text{ day}})^d}\right]. \tag{5.4}$$

As in Metzger (2017), although the constants are dependent on the layer, we take them to be $a = 0.56$, $b = 0.17$, $d = 0.74$. The radiated luminosity and energy are evolved according to (Metzger, 2017),

$$L(m) = \frac{E(m)}{t_{\text{diff}}(m) + t_{\text{lc}}(m)} \tag{5.5}$$

$$\frac{dE(m)}{dt} = -\frac{E(m)}{R(m)}\frac{dR(m)}{dt} - L(m) + \dot{Q}(m), \tag{5.6}$$

where $t_{\text{lc}}(m) = R(m)/c$ is the light crossing time, and t_{diff} is the diffusion timescale outward from mass coordinate m,

70
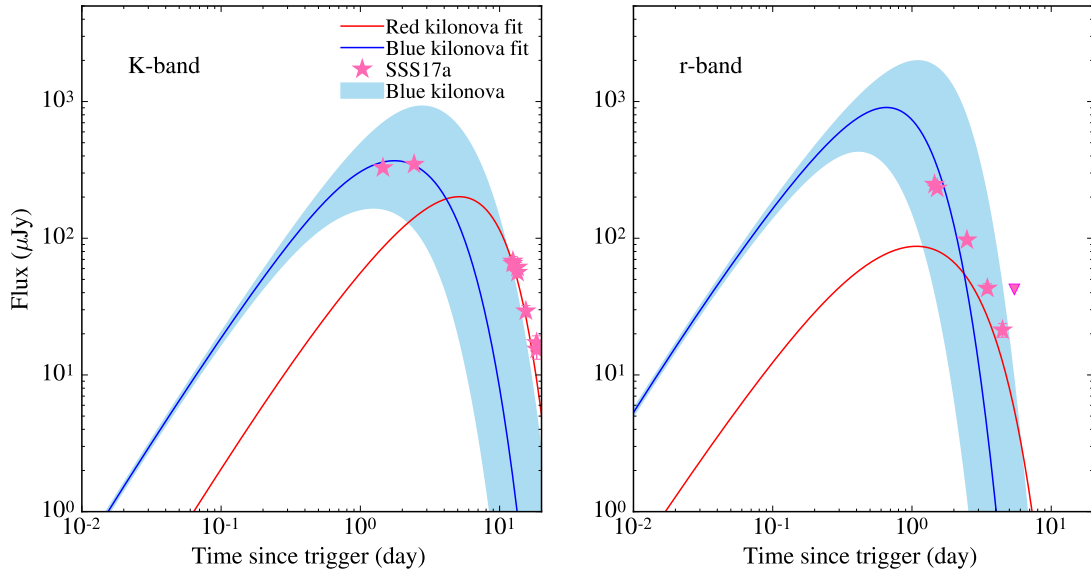
Figure 5.3: Reconstructed light curve evolution in the K (left) and r (right) bands for our inferred red to blue mass ratios. The one sigma contours are shown in light blue. The data points show the evolution of SSS17a/AT2017gfo lying within our abundance derived constraints (taken from Coulter et al. (2017a); Drout et al. (2017a); Kilpatrick et al. (2017)), and solid lines show the KN model with parameters inferred for GW170817. We consider GW170817 to be at a distance of 39.5 Mpc. The parameters for the red component of the KN are: $m_{\rm ej} = 0.035 M_\odot$, $v_{\rm ej} = 0.15c$ (Kilpatrick et al., 2017), $\kappa = 5$ cm^{2}g^{-1}. , and the blue component has $v_{\rm ej} = 0.3c$ and an opacity of $\kappa = 0.08$ cm^{2}g^{-1} (Drout et al., 2017a).

$$t_{\mathrm{diff}}(m) = \frac{3m\kappa(m)}{4\pi v(m)R(m)}. \tag{5.7}$$

As pointed out in Metzger (2017), the first term in the energy equation corresponds to adiabatic loss of energy due to expansion. Once the radiated luminosity is estimated for each layer, the total luminosity is calculated by adding the contribution of each layer. The radiation is assumed to be a black body, and have a photosphere where the ejecta becomes optically thin, i.e. where the optical depth $\tau = \frac{3m\kappa(m)}{4\pi R(m)^2} = 1$, so that the observed flux becomes

$$F_\nu = \frac{2\pi h\nu^3}{c^2} \frac{1}{\exp(h\nu/kT_{\mathrm{eff}}) - 1} \frac{R_{\mathrm{ph}}^2}{D^2}, \tag{5.8}$$

with a temperature

$$T_{\mathrm{eff}} = \left(\frac{L}{4\pi\sigma_{\mathrm{SB}}R_{\mathrm{ph}}^2} \right), \tag{5.9}$$

where D is the distance to the object, in the case of SSS17a/AT2017gfo, $D = 39.5$ Mpc.

We treat the KN as consisting of two distinct and non-interacting components, and the free parameters in the model are the mass, velocity, and opacity of each component We assume an inclination angle toward the observer in which both components are visible, though in reality unfavorable inclinations may affect the masses inferred (Kasen et al., 2017a). To transform from an observed stellar abundance ratio to an actual red/blue component mass, we "anchor" to the observed red component mass of SSS17a/AT2017gfo, $M_{\mathrm{red}} = 0.034\ M_\odot$. We then calculate an inferred blue component mass by multiplying by the inverse of the mass ratio. Figure 5.3 shows the ensemble properties of KNe inferred through this method. The one sigma contours of the lognormal distribution shown in Figure 5.2 mapped

through the KN model are shown by the blue contours. The observed evolution of SSS17a/AT2017gfo lies comfortably within the contours, serving as an initial validation of our assumptions.

5.5   Discussion

As shown in Figure 5.3, a significant diversity in KN evolution is to be expected under the assumption that NSMs provide the bulk of the r-process production in the early universe. This prediction holds great diagnostic power, as the role of NSMs serving as the only significant r-process producer throughout cosmic time has recently come into question due to the [Eu/Fe] trend showing a "knee" at an [Fe/H] metallicity of -1, hinting toward a mechanism which does not follow the t^{-1} delay time distribution characteristic of Type Ia supernovae and NSMs (Côté et al., 2018). One model which may satisfy this constraint is that of the collapsar (Woosley, 1993), in which a massive rotating star may form a remnant accretion disk around a black hole, successfully launching accretion disk winds in which a successful r-process may take place (Siegel et al., 2018), though in Chapter 4 we have called this model into question based on observations of r-process abundances in metal-poor stars.

This work provides an independent observational diagnostic for the role that NSMs may have in early r-process nucleosynthesis. As KNe will not soon be observable in the early universe, the distribution of inferred red and blue component masses can be compared against those seen in metal poor stars as an indirect test of their viability at early times. If our prediction is correct, we expect to see our inferred distribution filled out with observations of EM counterparts to NSMs. Strong deviation from this distribution would necessarily imply that some other significant source of r-process has enriched the r-process enhanced low metallicity

stars we observe.

Chapter 6

Conclusion

The future is remarkably bright for the study of progenitors of the r-process and the formation of compact binaries. As LIGO continues to secure the rates of NSMs and NSBH mergers and guide observations of their EM counterparts, we will inevitably be able to move the theoretical understanding of these events forward. In addition, dedicated surveys such as the r-process Alliance (Hansen et al., 2018; Sakari et al., 2018; Placco et al., 2019) expect to increase the sample size of highly enhanced r-process stars by a factor of four and continue to add to our knowledge of the conditions under which heavy elements are synthesized.

As mentioned throughout this thesis there remain several open questions regarding the topics discussed. Is the common envelope a dominant channel in forming the GW signals LIGO detects? How much of the galactic r-process content can NSMs account for? Do they operate robustly throughout cosmic time, and if not what mechanism does operate to create the low metallicity r-process enhanced stars? Are we in some way biased by observations of halo stars which may have an accretion origin, and if so how might that affect our conclusions?

It is possible that the answer to several of these questions may lie within existing stellar abundance data, and this thesis has largely focused on utilizing

these data to their fullest potential considering the extraordinary amount of work that has gone into collecting them. This is what I plan to spend the next several years doing, while being guided by observational results from surveys such as the r-process Alliance as well as LIGO detected compact mergers along the way. I am consistently humbled by the fact that I get to work on a question that can be posed as simply as "Where is gold made?", and to answer these fundamental questions with fundamental physics.

Bibliography

Abbott, B. P., Abbott, R., Abbott, T. D., et al. 2017a, ApJ, 848, L13

—. 2017b, Physical Review Letters, 119, 161101

—. 2017c, Physical Review Letters, 119, 161101

—. 2017d, ApJ, 848, L12

Abohalima, A., & Frebel, A. 2018, The Astrophysical Journal Supplement Series, 238, 36

Arcavi, I. 2018, ApJ, 855, L23

Arcones, A., & Montes, F. 2011, ApJ, 731, 5

Arnone, E., Ryan, S. G., Argast, D., Norris, J. E., & Beers, T. C. 2005, A&A, 430, 507

Arnould, M., Goriely, S., & Takahashi, K. 2007, Phys. Rep., 450, 97

Ascenzi, S., Coughlin, M. W., Dietrich, T., et al. 2019, MNRAS, 486, 672

Audouze, J., & Silk, J. 1995, ApJ, 451, L49

Barklem, P. S., Christlieb, N., Beers, T. C., et al. 2005, A&A, 439, 129

Barnes, J., & Kasen, D. 2013, ApJ, 775, 18

Barnes, J., Kasen, D., Wu, M.-R., & Martínez-Pinedo, G. 2016, ApJ, 829, 110

Bauswein, A., Ardevol Pulpillo, R., Janka, H. T., & Goriely, S. 2014, ApJ, 795, L9

Bauswein, A., Goriely, S., & Janka, H.-T. 2013, ApJ, 773, 78

Behroozi, P. S., Ramirez-Ruiz, E., & Fryer, C. L. 2014, ApJ, 792, 123

Belczynski, K., Perna, R., Bulik, T., et al. 2006, ApJ, 648, 1110

Beniamini, P., Hotokezaka, K., & Piran, T. 2016a, ApJ, 829, L13

—. 2016b, ArXiv e-prints, arXiv:1608.08650

Beun, J., McLaughlin, G. C., Surman, R., & Hix, W. R. 2008, Phys. Rev. C, 77, 035804

Burbidge, E. M., Burbidge, G. R., Fowler, W. A., & Hoyle, F. 1957, Rev. Mod. Phys., 29, 547

Cameron, A. G. W. 1957, PASP, 69, 201

Cayrel, R., Depagne, E., Spite, M., et al. 2004, A&A, 416, 1117

Cioffi, D. F., McKee, C. F., & Bertschinger, E. 1988, ApJ, 334, 252

Côté, B., Eichler, M., Arcones, A., et al. 2018, arXiv e-prints, arXiv:1809.03525

Coulter, D. A., Foley, R. J., Kilpatrick, C. D., et al. 2017a, Science, 358, 1556

—. 2017b, Science, 358, 1556

Cowan, J. J., & Thielemann, F.-K. 2004, Physics Today, 57, 47

Cowperthwaite, P. S., Berger, E., Villar, V. A., et al. 2017, ApJ, 848, L17

Cyburt, R. H., Amthor, A. M., Ferguson, R., et al. 2010, ApJS, 189, 240

Darwin, G. H. 1879, Proceedings of the Royal Society of London Series I, 29, 168

Drout, M. R., Piro, A. L., Shappee, B. J., et al. 2017a, Science, 358, 1570

—. 2017b, Science, 358, 1570

Duchêne, G., & Kraus, A. 2013, ARA&A, 51, 269

Eichler, D., Livio, M., Piran, T., & Schramm, D. N. 1989, Nature, 340, 126

Fields, B. D., Truran, J. W., & Cowan, J. J. 2002, ApJ, 575, 845

Frebel, A. 2018, Annual Review of Nuclear and Particle Science, 68, 237

Freiburghaus, C., Rosswog, S., & Thielemann, F.-K. 1999, ApJ, 525, L121

Frischknecht, U., Hirschi, R., Pignatari, M., et al. 2016, MNRAS, 456, 1803

Fulbright, J. P., Wyse, R. F. G., Ruchti, G. R., et al. 2010, ApJ, 724, L104

Gompertz, B. P., Levan, A. J., Tanvir, N. R., et al. 2018, ApJ, 860, 62

Goriely, S., Bauswein, A., & Janka, H.-T. 2011, ApJ, 738, L32

Greif, T. H., Glover, S. C. O., Bromm, V., & Klessen, R. S. 2009, MNRAS, 392, 1381

Grossman, D., Korobkin, O., Rosswog, S., & Piran, T. 2014, MNRAS, 439, 757

Hansen, T. T., Holmbeck, E. M., Beers, T. C., et al. 2018, ApJ, 858, 92

Honda, S., Aoki, W., Ishimaru, Y., Wanajo, S., & Ryan, S. G. 2006, ApJ, 643, 1180

Hotokezaka, K., Piran, T., & Paul, M. 2015, Nature Physics, 11, 1042

Iglesias, C. A., & Rogers, F. J. 1996, ApJ, 464, 943

Ivanova, N., Justham, S., & Podsiadlowski, P. 2015, MNRAS, 447, 2181

Ivanova, N., Justham, S., Chen, X., et al. 2013, A&A Rev., 21, 59

Ji, A. P., Frebel, A., Chiti, A., & Simon, J. D. 2016a, Nature, 531, 610

—. 2016b, Nature, 531, 610

Ji, A. P., Frebel, A., Ezzeddine, R., & Casey, A. R. 2016c, ApJ, 832, L3

Ji, A. P., Frebel, A., Simon, J. D., & Chiti, A. 2016d, ArXiv e-prints, arXiv:1607.07447

Kasen, D., Metzger, B., Barnes, J., Quataert, E., & Ramirez-Ruiz, E. 2017a, Nature, 551, 80

—. 2017b, Nature, 551, 80

Kelley, L. Z., Ramirez-Ruiz, E., Zemp, M., Diemand, J., & Mandel, I. 2010, ApJ, 725, L91

Kilpatrick, C. D., Foley, R. J., Kasen, D., et al. 2017, Science, 358, 1583

Kobayashi, C., Umeda, H., Nomoto, K., Tominaga, N., & Ohkubo, T. 2006, ApJ, 653, 1145

Korobkin, O., Rosswog, S., Arcones, A., & Winteler, C. 2012, MNRAS, 426, 1940

Kruckow, M. U., Tauris, T. M., Langer, N., et al. 2016, A&A, 596, A58

Kurtenkov, A. A., Pessev, P., Tomov, T., et al. 2015, A&A, 578, L10

Lattimer, J. M., & Schramm, D. N. 1974a, ApJ, 192, L145

—. 1974b, ApJ, 192, L145

Law-Smith, J., MacLeod, M., Guillochon, J., Macias, P., & Ramirez-Ruiz, E. 2017, ApJ, 841, 132

Lee, W. H., & Ramirez-Ruiz, E. 2006, ApJ, 641, 961

Lejeune, T., Cuisinier, F., & Buser, R. 1997, A&AS, 125, 229

—. 1998, A&AS, 130, 65

Li, L.-X., & Paczyński, B. 1998, ApJ, 507, L59

Lodders, K. 2003, ApJ, 591, 1220

Lopez, L. A., Ramirez-Ruiz, E., Huppenkothen, D., Badenes, C., & Pooley, D. A. 2011, ApJ, 732, 114

MacFadyen, A. I., & Woosley, S. E. 1999, ApJ, 524, 262

Macias, P., & Ramirez-Ruiz, E. 2018, ApJ, 860, 89

—. 2019, arXiv e-prints, arXiv:1905.04315

MacLeod, M., Antoni, A., Murguia-Berthier, A., Macias, P., & Ramirez-Ruiz, E. 2017a, ApJ, 838, 56

MacLeod, M., Macias, P., Ramirez-Ruiz, E., et al. 2017b, ApJ, 835, 282

MacLeod, M., Ostriker, E. C., & Stone, J. M. 2018, ApJ, 863, 5

MacLeod, M., & Ramirez-Ruiz, E. 2015, ApJ, 803, 41

Maeda, K., & Nomoto, K. 2003, ApJ, 598, 1163

Martin, D., Perego, A., Arcones, A., et al. 2015, ApJ, 813, 2

Martizzi, D., Faucher-Giguère, C.-A., & Quataert, E. 2015, MNRAS, 450, 504

Metzger, B. D. 2017, Living Reviews in Relativity, 20, 3

Metzger, B. D., Margalit, B., Kasen, D., & Quataert, E. 2015, MNRAS, 454, 3311

Metzger, B. D., Thompson, T. A., & Quataert, E. 2018, ApJ, 856, 101

Metzger, B. D., Martínez-Pinedo, G., Darbha, S., et al. 2010a, MNRAS, 406, 2650

—. 2010b, MNRAS, 406, 2650

Montes, F., Beers, T. C., Cowan, J., et al. 2007, ApJ, 671, 1685

Montes, G., Ramirez-Ruiz, E., Naiman, J., Shen, S., & Lee, W. H. 2016, ArXiv e-prints, arXiv:1601.05808

Mösta, P., Roberts, L. F., Halevi, G., et al. 2018, ApJ, 864, 171

Murguia-Berthier, A., MacLeod, M., Ramirez-Ruiz, E., Antoni, A., & Macias, P. 2017, ApJ, 845, 173

Naiman, J. P., Pillepich, A., Springel, V., et al. 2018, MNRAS, arXiv:1707.03401

Nicholls, C. P., Melis, C., Soszynski, I., et al. 2013, MNRAS, 431, L33

Nishimura, N., Takiwaki, T., & Thielemann, F.-K. 2015, ApJ, 810, 109

Nomoto, K., Tominaga, N., Umeda, H., Kobayashi, C., & Maeda, K. 2006, Nuclear Physics A, 777, 424

Paczynski, B. 1976, in IAU Symposium, Vol. 73, Structure and Evolution of Close Binary Systems, ed. P. Eggleton, S. Mitton, & J. Whelan, 75

Paxton, B., Bildsten, L., Dotter, A., et al. 2011, ApJS, 192, 3

Paxton, B., Cantiello, M., Arras, P., et al. 2013, ApJS, 208, 4

Paxton, B., Marchant, P., Schwab, J., et al. 2015, ApJS, 220, 15

Pignatari, M., Gallino, R., Meynet, G., et al. 2008, ApJ, 687, L95

Piro, A. L., & Kollmeier, J. A. 2018, ApJ, 855, 103

Placco, V. M., Santucci, R. M., Beers, T. C., et al. 2019, ApJ, 870, 122

Qian, Y.-Z., & Wasserburg, G. J. 2007, Phys. Rep., 442, 237

Radice, D., Perego, A., Hotokezaka, K., et al. 2018a, ApJ, 869, 130

—. 2018b, ApJ, 869, 130

Ramirez-Ruiz, E., & MacFadyen, A. I. 2010, ApJ, 716, 1028

Ramirez-Ruiz, E., Trenti, M., MacLeod, M., et al. 2015, ApJ, 802, L22

Reddy, B. E., Lambert, D. L., & Allende Prieto, C. 2006, MNRAS, 367, 1329

Reddy, B. E., Tomkin, J., Lambert, D. L., & Allende Prieto, C. 2003, MNRAS, 340, 304

Reimers, D. 1975, Memoires of the Societe Royale des Sciences de Liege, 8, 369

Roberts, L. F., Kasen, D., Lee, W. H., & Ramirez-Ruiz, E. 2011a, ApJ, 736, L21

—. 2011b, ApJ, 736, L21

Roederer, I. U., Hattori, K., & Valluri, M. 2018, AJ, 156, 179

Roederer, I. U., Preston, G. W., Thompson, I. B., et al. 2014, AJ, 147, 136

Rosswog, S., Liebendörfer, M., Thielemann, F.-K., et al. 1999a, A&A, 341, 499

—. 1999b, A&A, 341, 499

Rucinski, S. M. 1998, AJ, 115, 1135

Safarzadeh, M., Ramirez-Ruiz, E., Andrews, J. J., et al. 2019, ApJ, 872, 105

Sakari, C. M., Placco, V. M., Farrell, E. M., et al. 2018, ApJ, 868, 110

Shappee, B. J., Simon, J. D., Drout, M. R., et al. 2017, Science, 358, 1574

Shen, S., Cooke, R. J., Ramirez-Ruiz, E., et al. 2015, ApJ, 807, 115

Shigeyama, T., & Tsujimoto, T. 1998, ApJ, 507, L135

Siegel, D. M. 2019, arXiv e-prints, arXiv:1901.09044

Siegel, D. M., Barnes, J., & Metzger, B. D. 2018, arXiv e-prints, arXiv:1810.00098

Siegel, D. M., Barnes, J., & Metzger, B. D. 2019, Nature, 569, 241

Simmerer, J., Sneden, C., Cowan, J. J., et al. 2004, ApJ, 617, 1091

Simonetti, P., Matteucci, F., Greggio, L., & Cescutti, G. 2019, MNRAS, 978

Sluder, A., Ritter, J. S., Safranek-Shrader, C., Milosavljević, M., & Bromm, V. 2016, MNRAS, 456, 1410

Sneden, C., Cowan, J. J., & Gallino, R. 2008, ARA&A, 46, 241

Soker, N. 2017, MNRAS, 471, 4839

Suda, T., Katsuta, Y., Yamada, S., et al. 2008, PASJ, 60, 1159

Surman, R., Mumpower, M., Sinclair, R., et al. 2014, AIP Advances, 4, doi:http://dx.doi.org/10.1063/1.4867191

Thornton, K., Gaudlitz, M., Janka, H.-T., & Steinmetz, M. 1998, ApJ, 500, 95

Travaglio, C., Gallino, R., Arnone, E., et al. 2004, ApJ, 601, 864

Tylenda, R., Hajduk, M., Kamiński, T., et al. 2011, A&A, 528, A114

van de Voort, F., Quataert, E., Hopkins, P. F., Kereš, D., & Faucher-Giguère, C.-A. 2015, MNRAS, 447, 140

Venn, K. A., Irwin, M., Shetrone, M. D., et al. 2004, AJ, 128, 1177

Villar, V. A., Berger, E., Metzger, B. D., & Guillochon, J. 2017, ApJ, 849, 70

Waxman, E., Ofek, E. O., Kushnir, D., & Gal-Yam, A. 2018, MNRAS, 481, 3423

Williams, S. C., Darnley, M. J., Bode, M. F., & Steele, I. A. 2015, ApJ, 805, L18

Wilson, E. C., & Nordhaus, J. 2019, MNRAS, 485, 4492

Winteler, C., Käppeli, R., Perego, A., et al. 2012, ApJ, 750, L22

Woosley, S. E. 1993, ApJ, 405, 273

Woosley, S. E., & Weaver, T. A. 1995, ApJS, 101, 181

Woosley, S. E., Wilson, J. R., Mathews, G. J., Hoffman, R. D., & Meyer, B. S. 1994, ApJ, 433, 229

Wu, M.-R., Fernández, R., Martínez-Pinedo, G., & Metzger, B. D. 2016a, MNRAS, 463, 2323

—. 2016b, MNRAS, 463, 2323